Detection of Old Diffusive Windthrow Using Low Cost Resources. the Case of Xynthia Storm in the Vosges Mountains, 28 February 2010

Ionel Haidu, Paula Furtuna, Sébastien Lebaut

 doi:10.20944/preprints201709.0038.v1

Article

Detection of Old Diffusive Windthrow Using Low Cost Resources. the Case of Xynthia Storm in the Vosges Mountains, 28 February 2010

Ionel Haidu[1]*, Paula Furtuna[2]* and Sébastien Lebaut[1],

[1] Laboratoire LOTERR-EA7304, Université de Lorraine, 57045 Metz Cedex 01, France; ionel.haidu@univ-lorraine.fr, sebastien.lebaut@univ-lorraine.fr
[2] Faculty of Geography, Babes Bolyai Univesity, 400334 Cluj-Napoca, Romania; paula_roxana.furtuna@yahoo.com
* Correspondence: ionel.haidu@univ-lorraine.fr Tel.: +33-605-984-480; paula_roxana.furtuna@yahoo.com Tel.: +40-754-493-296

Abstract: Unlike the contiguous windthrows, the diffuse windthrows occurred as a result of wind gusts of lower speed (100-140 km/h) than in the first case (>140 km/h) are much more difficult to detect due to their much lower areas and due to their very large number, of several hundreds in the wooded mountain massifs. The objective of this research is to present a rapid procedure for the detection of the diffuse windthrows based on low cost, Landsat type images, knowing that certain sensors cannot be accessed without significant investments. Our application is based on the study of effects caused by the Xynthia storm in the Vosges Mountains in the North-East of France, on 28 February 2010. Thus, based on two sets of Landsat satellite images, we used the "dark object" approach and the Disturbance Index, as well as a classification of the images before and after the storm, resulting in a change map. Following the detection process, 257 scattered polygons were detected, totalling 229 ha. For validation purposes, high-resolution images and orthophotoplans taken before and after storm were used. The error matrix was calculated, achieving an overall accuracy of 86%, which confirms the quality of our analysis and supports this procedure for detecting diffuse windthrow based on low cost resources.

Keywords: windthrow; Xynthia storm; Landsat imagery; limited data.

1. Introduction

Storms are known to be the most destructive natural disasters for forests in terms of frequency of occurrence, damages caused and their spatial extent [1,2,3]. Such a meteorological phenomenon occurring in France was the Xynthia storm, on 28 February 2010. Although it did not have the exceptional nature of the catastrophic Lothar storm in 1999 [4,5] or Klaus storm in 2009 [6] by its maximum speed (160 km/h), it caused major damages, i.e. thousands of cubic meters of forest destroyed in Lorraine and Alsace. The Pôle interrégional de la Santé des Forêts du Nord-Est Institute [7,8] mentions for the Lorraine region some 15,000 m^3 of destabilized spruce at Louppy-sur-Loison (department of Meuse), some pine forests in the Wardnt Plateau (department of Moselle), and, to a lesser extent, some aged beech forests. In the Alsace region, the same source mentions some limited destabilization in forest border areas or in areas where there is no longer any interest in logging. Besides the official reports [9,10,11,12] the press of the time, i.e. The Vosges Martin newspaper, LOR'Actu, France Culture, but also other local and regional media sources have presented more dramatically the effects of this storm on the forests of Vosges, suggesting that many more points would have been affected, as the windthrow had a diffuse character [13,14]. Even if several years

have passed since that event, through remote sensing images that stored the condition of vegetation, in this paper we will try to identify the affected points that seem to be masked by the extent of the forest crop.

The detection of the changes caused by storms, be they contiguous or diffused, is very important in order to establish spatial and temporal trends in the rehabilitation and management of forest resources. Papaik and Canham [15] show that storms can be seen as an integral part of the forest ecosystems functioning, but that the detection of changes must be conducted in order to know and manage ecosystems and forest resources. The use of remote sensing in forestry applications is today an extremely useful tool to acquire knowledge and conduct the management of forest ecosystems. The information provided by this tool on the interaction between the atmosphere and the forest for the purpose, for example, of locating the damages caused by storms in the context of climate change [16,17,18,19] or for carbon sequestration potential [20,21] is a must because it can help extrapolate this information to larger spatial scales.

Huang et al. [22], proposed a method for the detection of forest areas affected by storms, the use of vegetation indices and the Tasselled Cap Transformation. Based on this transformation, Healey et al. [23] developed the Disturbance Index, used for windthrow detection. The idea behind the index is that disturbance sites exhibit higher brightness, and lower greenness and wetness values compared to the undisturbed forests [24]. This procedure was then optimized and adapted to the purpose of continual monitoring of forest disturbances through time series images [25,26,27,28].

Another direction for the development of remote sensing to identify windthrows refers to semi-automatic or automatic procedures. Stach et al. [29] proposed mapping by optical and radar remote sensing. Huang et al. [30] developed dark object concept and support vector machines to automate forest cover change analysis, while Kennedy et al. [31] used LandTrendr segmentation algorithms in order to develop maps of forest disturbance and regrowth.

Regarding the methodology applied to assess the consequences of Martin and Lothar hurricanes in 1999 on the forests of France, Stach et al. [32] concluded that the best results were those achieved by radar remote sensing.

Due to the meteorological risk events causing significant damages throughout recent decades, France, but also other countries in Western Europe experienced large windthrow areas. Therefore, the researchers from the French National Forest Inventory [6,33] have developed a new semi-automatic methodology, the "7 point method" to map the felling damages caused by the storms and to monitor the land use adapted to varied landform conditions. The principle of the method is based on the "pixel per pixel" comparison of two satellite images recorded before and after the storm. The "pixel per pixel" and "spectral band with spectral band" difference is performed to highlight the radiometric evolution between the images before and after the storm. In order to detect the windthrows, the "7-point method" combines the change detection techniques with an automatic image segmentation phase, namely the delimitation of homogeneous areas in terms of radiometry and texture. The detected forest changes caused by the storm are highlighted, the damages identified in each plot are classified and, in the end, the damage map for the analysed area is obtained by combining all the previous results. This methodology has been used to map the windthrows and damages caused by the Lothar and Martin storms in 1999 in Forêt des Landes, South-Western France. The windthrow mapping in the Vosges department in the year 2002 was carried out by combining remote sensing for the plain and hill areas with aerial photogrammetry for the mountain [33]. The forest damages caused by the Klaus storm occurring in January 2009 were also evaluated using the 7-point method [6]. The working principle of these methods is the achievement of real-time information by transforming the remote sensing images into vegetation state indices needed to identify the disturbances or abnormalities occurring in the forest areas [34].

The wider and wider use of very high-resolution (VHR) remotely sensed images has stimulated the development of object-based methods and data mining techniques, which were much more effective for change detection [35]. Bauman et al. [24] have developed a methodology for detecting and analysing windthrows for various meteorological phenomena. Moreover, they have managed to separate the disturbances due to the storms as compared to those caused by massive forest cuttings

 doi:10.20944/preprints201709.0038.v1

in the forest areas, as well as to the other land cover classes. This study was implemented in a temperate zone in Russia and in an area in the USA boreal forests. The methodology applied in this study was based on the detection of windthrows using the Disturbance Index that was designed considering the Tasselled Cap transformation and the "dark object" approach.

The purpose of our application is to detect the forest areas in the Vosges Mountains affected by the Xynthia storm in February 2010, as it is well known that there are diffuse windthrows, without taking into account more sophisticated but also more expensive imaging resources, such as those mentioned above, but, on the contrary, using Landsat's least expensive satellite imagery.

2. The study area and the storm event

The study area is represented by the Vosges Mountains (7,360 km^2, of which 4,400 km^2 are forest area), located in the North-Eastern part of France (Figure 1), in low altitude mountains, with 14 peaks exceeding 1,000 m and the maximum altitude, of 1,424 m, in the Grand Ballon Peak. The mountains expand longitudinally over approximately 200 km until the German border, along the west bank of the Rhine River. Their maximum width is 60 km in the South, 20 km in the North and only 4 km in their upper third part. The Southern part of the massif consists in crystalline schists, while the Northern part is composed largely of sandstones. The lithology of the area has been heavily influenced by glacial erosion, with many glacial lakes being found here.

Due to the geographic location, the Vosges Mountains experience two climate influences: oceanic and semi-continental. West from the Vosges Mountains, the relief has lower altitudes (Parisian Basin and Lorrain Plateau). Therefore, the air masses propelled by the oceanic disturbances are forced to escalate the Western flanks of the Vosges Mountains generating severe weather conditions and strong wind gusts. However, the storms in the Vosges are not as severe or devastating as those on the Atlantic coast, although they are reactivated by the escalation of the mountains. This is because they weaken in intensity due to the distance of about 1,000 km that these storms have to pass through until the North-East of France, in the exit area from the French territory. The dominant winds are in the Western sector, and in case of storms such as Lothar on 26 December 1999 and Xynthia on 28 February 2010, blow in gusts exceeding 170 km/h on the mountains peaks. This was also the case of some tornadoes, such as the one on 11 July 1984, when some extremely strong gusts were recorded, of 200 km/h.

The massif is predominantly covered by forest (60% of the surface of the mountains today), especially conifers (pine and spruce), which is up to the altitude of 800-1000 m, while towards the foothills of the mountains there is a transition to deciduous forests, as well as to open meadows that were created by man for agricultural practices. The forest cover of the Vosges Mountains ranks second in France in terms of extent, after the Landes forest. It covers the East of Lorraine, the Alsace mountain region and the North-East of the Franche Comté region. The Vosges forest is the first region of France in terms of pine, fir and spruce production, with a crop of 1.5 million m^3 of logs, namely 1/3 of the country's total production. Without the human intervention, with the most intense deforestations in the 18th and 19th centuries, the forest would have covered the entire mountain area, except the highest peaks and areas exposed to the weather. Nowadays, the authorities apply the sustainable management principle, so that despite the significant harvest, the forest of Vosges is progressing, the annual harvest being much lower than the growth rate [6].

It is worth mentioning that the Vosges Mountains host 2 regional natural parks (Parc Naturel Régional des Vosges du Nord, Parc Naturel Régional des Ballons des Vosges), Réserve de biosphère transfrontalière des Vosges du Nord-Pfälzerwald (France-Germany), as well as some national natural reserves related to the presence of the forest.

But sometimes weather conditions are so severe that trees are broken or uprooted. The most frequent and extensive windthrows in the Vosges Mountains were caused by wind gusts either due to tornadoes formed during some hot summers or due to winter storms.

The tornadoes monitoring and research group Keraunos, Meteo France, as well as the historical contributions of the CLI.M.A.57-67-68 association and the works of Garnier [37] and [38], enable us

Preprints (www.preprints.org) | NOT PEER-REVIEWED | Posted: 11 September 2017 doi:10.20944/preprints201709.0038.v1

to list the most devastating tornadoes mentioned for the Vosges: 13.08.1770 at Gérardmer, 29.05.1807 at Lusse, 11.06.1880 at Eloyes, 10.07.1968 a tornado in the Eastern part of Lorraine, 30.06.2012 at Gérardmer and 13.05.2015 at Gerbépal. It is worth mentioning that most often such tornadoes or mini-tornadoes are produced in the Western part of the Vosges Mountains. In remote sensing studies careful consideration should be given when selecting images for the consequences of certain episodes with wind gusts in order to avoid confusion and to correctly identify the cause of windthrows, be they summer tornadoes or winter storms.

A very violent convective phenomenon similar to a mini-tornado called "derecho" occurred on 16 September 2015 in the Centre and East of France, which affected also the Western part of the Vosges Mountains and caused significant windthrows. Even in the winters with remarkable snowfalls (1969/1970, 1994/1995, 2005/2006) some trees were damaged or blown over by "heavy snow", sometimes in combination with a stronger wind. Rarely, in the case of sudden snow removal, stone and mud torrents can be formed that damage or break trees in their path.

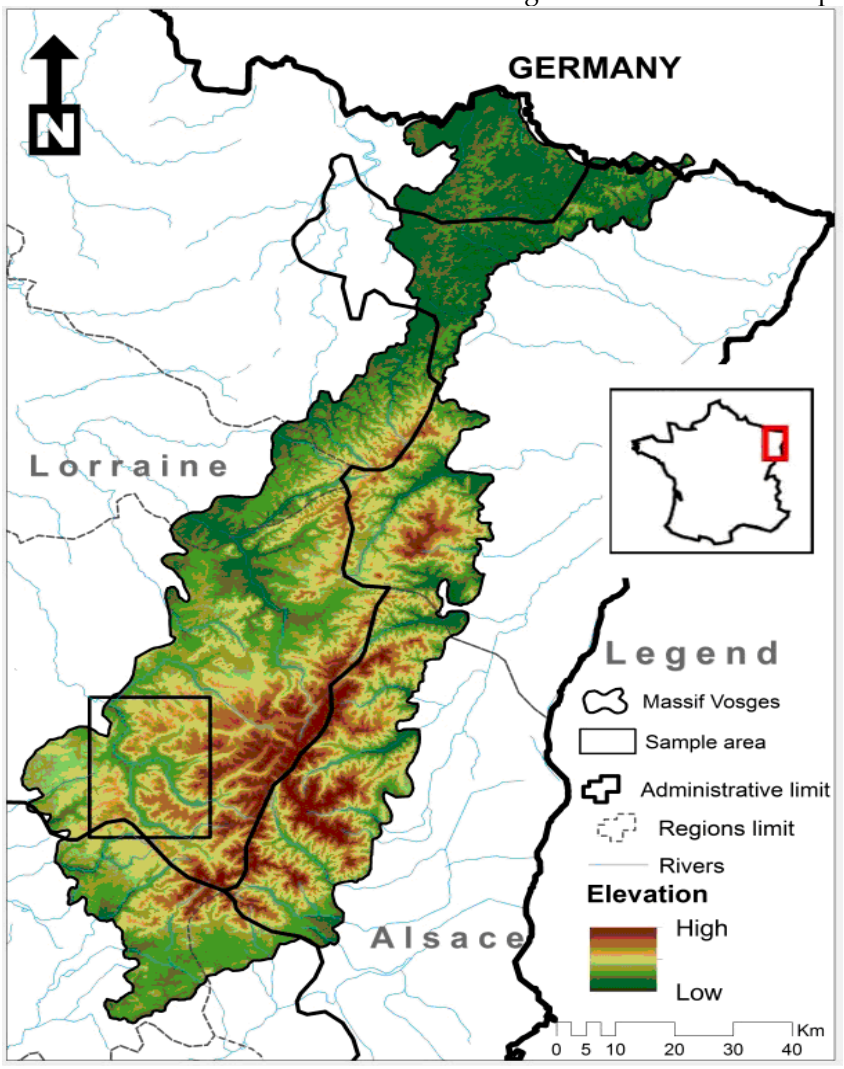

Figure 1. Location of Vosges Mountains and a sample area highlighted later.

Due to location, climatic conditions and topography, the Vosges Mountains area has often been affected by major winter storms that have led to windthrows on extensive forest areas, causing the greatest damages if we also relate to other damaging causes for forests. Meteo France distinguishes 12 types of storms, [39] with the most frequent being the North and West oceanic storms. Hence, the Vosges Mountains area, especially the Northern part, is on the storm's travel path. Obviously, the French coastline is the most exposed and feels the maximum strength of any storm originating in the Atlantic. Then, the storm's strength gradually weakens towards the interior of the country. This

 doi:10.20944/preprints201709.0038.v1

explains why windthrows in the North-Eastern France and the ones from the Vosges Mountains have a local character or are often diffuse.

The Xynthia winter storm occurred from a low pressure system formed in the subtropical area south of the Azores on 25 February 2010. The southern flow of cold air masses from the altitude caused the formation of a depression over the Centre and Eastern part of the North Atlantic Ocean. The high temperature difference between the extremely hot air flow above the Africa and the cold air in the Eastern Atlantic Ocean has accentuated the decrease in atmospheric pressure that led to the formation of the powerful Xynthia cyclone. The cyclone experienced a rapid intensification affecting 8 countries, and causing 65 deaths [40] in its movement from SW to NE (Figure 2). The depression core reached the Gascogne Bay on the evening of 27 February bringing violent winds from the Southern sector that blew in the Pyrenees Mountains at 242 km/h. On the morning of 28 February, Xynthia furiously hit the French coastline, the pressure at the centre of the cyclone dropped to 968 hPa and the wind gusts reached 120-160 km/h. Following its path, Xynthia crossed the South-West and Central France, approaching the Vosges Mountains from the South-West direction on 28 February 2010. Wind gusts of 172 km/h were recorded in the Markstein Resort (68) located at 1184 m altitude, but also the other mountain or resorts in the neighbourhood of the Vosges Mountains recorded notable wind gusts: Septsarges (55) 147 km/h, Goin (57) 136 km/h, Metz (57) 136 km/h, Belmont (67) 134 km/h, and Vagney (88) 133 km/h. According to the classification cited above, Xynthia was of the SW type, with an extremely southern origin (close to the Tropic of Cancer) for a typical winter storm. It had an atypical trajectory and its effect was felt in North-Eastern France exceeding its borders, until the Baltic Sea, which showed that winter storms could threaten the entire country. From a statistical point of view, Bedach and Hofherr [40] estimate that storms as severe as Xynthia have an average occurrence frequency in France once every two years.

The existing literature [4,37,38,39,41,42] allowed us to locate Xynthia in a series of devastating storms that have hit the Vosges Mountains (Table 1).

Table 1. The main recorded winter storms that caused windthrows in the Vosges Mountains

Date	Affected area	Notable characteristics
1698	N-E of France	
1716	N-E of France	
1739, 14-18.01	N-E of France	Major forest damage in the Vosges Mountains
1836, 23.03	All France	
1866, 10-11.01	1866, 10-11.01	
1879, 20.02	All France	130 km/h gusts, Meurthe-et-Moselle very affected
1882, 26-27.03	All France	
1886, 27.02	N-E France	
1892, 29-30.03	Alsace	0,5 M m³ felled trees
1896, 04.12	N-E France	
1900, 13.02	Lorraine	
1902, 31.01-01.02	Vosges	2,2 M m³ felled trees
1920, 10-14.01	Moselle, Alsace	1,0 M m³ felled trees
1924, 08.10	N-E France	
1935, 22-23.02	N-E France	
1940, 14.03	Lorraine	180 km/h wind gusts in Nancy
1952, 12-13.12	Lorraine, Alsace	112 km/h wind gusts in Metz-Frescaty, major windthrows
1958, 02	Vosges	1.2 M m3 felled trees
1962, 16.02	Lorraine, Alsace	151 km/h wind gusts at Metz
1967, 02	N-E of France	130 km/h wind gusts at Bale-Moulhouse; 3.6 M m³ felled trees
1990, 25.01	N-E of France	DARIA storm, 137 km/h wind gusts at Nancy-Ochey
1990, 03.02	Almost all France	HERTA storm

Preprints (www.preprints.org) | NOT PEER-REVIEWED | Posted: 11 September 2017 doi:10.20944/preprints201709.0038.v1

1990, 26-28.02	Almost all France	VIVIANE storm
1990, 03	Lorraine, Alsace	WIEBKE storm, 144 km/h wind gusts at Metz
1994, 28.01	Landes, Alsace	1.2 M m³ felled trees
1999, 26-28.12	All France	LOTHAR storm, 155 km/h wind gusts at Nancy, 140 M m³ felled trees from which Lorraine 29.5 and Alsace 6.5
2006, 03.10	Alsace	RENATE storm, 149 km/h wind gusts at Markstein
2006,08.12	Alsace	VERA storm, 136 km/h wind gusts at Markstein
2009, 9-10.02	Alsace	QUINTEN storm, 166 km/h wind gusts at Markstein
2010, 28.02	Almost all France	XYNTHIA storm
2011, 15-18.12	N of France	JOACHIM storm, 192 km/h wind gusts at Markstein, limited windthrows, dispersed in the coniferous massifs
2013, 27-28.10	N-E of France	CHRISTIAN storm, 162 km/h wind gusts at Markstein
2014, 13.02	N-E of France	TINI II storm, 151 km/h wind gusts at Markstein, 17,000 m³ diffuse windthrows

As Bock et al. [43] stated, the institutes in France involved in the management of the forest resources - ONF (Office National des Foręts), IDF (Institut pour le Développement Forestier) and the INRA (Institut National pour la Recherche Agronomique), have studied the dependence between windthrows and wind speed. In regular beech forests, isolated windthrows occur at a wind speed ranging between 100 and 120 km/h, multiple diffuse windthrows occur at a 120-140 km/h wind speed, and large scale and frequent windthrows occur at speeds over 140 km/h. The same authors also found that at the height of the trees below 23-24 m the windthrows were rarer, but at wind speeds over 120 km/h the frequency of windthrows increased proportionally to the height of trees.

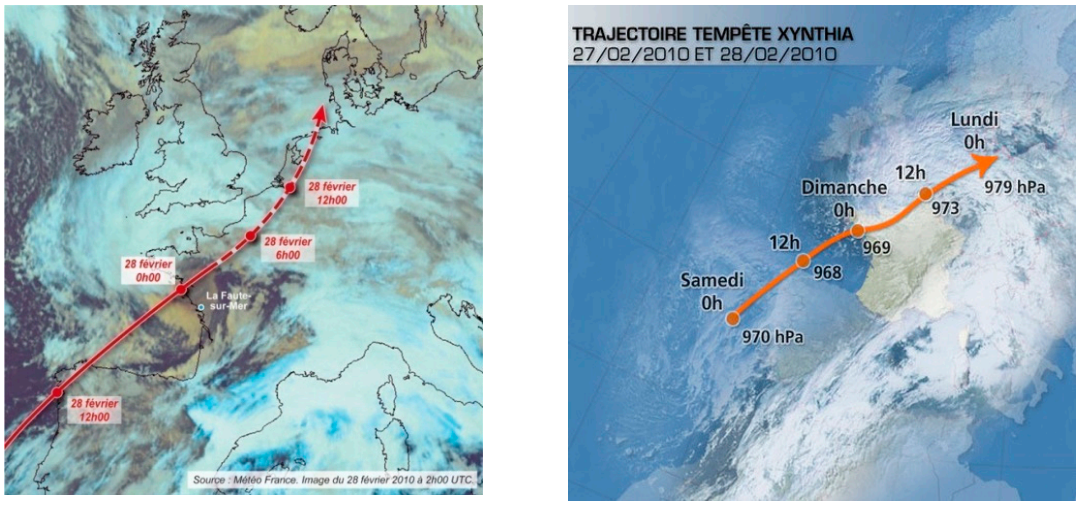

Figure. 2. The trajectory of the Xythhia storm, (source [39])

3. The alternative of using low cost resources

Nowadays, in the context of the impetuous development of remote sensing techniques, there is a natural preference for high and very-high-resolution (VHR) remote sensing images. Unfortunately, these are expensive and more difficult to access. We also have to admit that sometimes it is not possible to capture real-time images or create time series of images. Maybe this would be possible, but the cost of raw data purchases is too high. Therefore, we would like to assess if less expensive and easier-to-acquire images, such as Landsat, despite their lower resolution, would still be sufficient and capable of detecting diffuse windthrows. Starting with 2014 Sentinel Radar images are also free, but obviously these cannot be considered because the event we studied occurred in 2010. One should mention that in the case of the free images, very expensive software is often needed to process them.

 doi:10.20944/preprints201709.0038.v1

But if the purpose of a research is to rebuild the old windthrow trees, obviously, only the sources produced by the older satellites or having an archive (Landsat from 1980) can be accessed.

The availability of satellite data varies and choosing the best sensor is very important in order to select the data which better suit our purpose and to get more accurate results. When detecting windthrows using optical satellite imagery it is important to know which sensor is appropriate. Schwarz et al. [44] summarized the criteria to be considered in choosing the appropriate sensor, namely: *data availability*, *spectral resolution*, *spatial resolution* and *temporal resolution* (to increase the probability of achieving useful cloud-free data). Besides availability and resolution, the cost of data represents also an important factor to be considered. Satellite imagery products vary in their spatial and spectral resolution, geographic and temporal coverage, cloud cover, security regulations, and price [45]. The most frequently used and inexpensive data sources for detecting windthrows are the remote sensing images offered by the Landsat sensor [48]. These are basic sources due to the free of charge images and to the spatial, spectral and temporal details they provide for the mapping of the area damaged by storms.

The free of charge availability of Landsat archive and the large geographic coverage provide the opportunities to conduct studies over a long period of time and over a large area [47-49]. Beside the medium resolution provided, Landsat images at a spatial resolution of 30 m were successfully used to detect windthrows in various areas [23,24,27,50-53]. However, the increasing availability of high-resolution satellite imagery offers the potential to acquire data with fine spatial resolution (e.g. WorldView, Ikonos, Quickbird), but the cost of these data is a hindering factor in using them. Jackson et al. [54] showed that high-resolution imagery, like LIDAR, offered a great potential to detect windthrows, but they required more basic operating instructions.

In this study we chose to use Landsat data to detect the windthrows along the Vosges Mountains. The first reason in choosing Landsat sensor was the wide swath and the low cost. The medium resolution Landsat data is not as sharp as high-resolution images, but the amount of information it contains along with the large area coverage make this data suitable for large- or small-scale studies. We studied the diffuse windthrows and the exact location of these disturbances was unknown. Therefore, the availability and the coverage represented another factor in choosing the sensor. The Landsat TM and ETM+ program covers the entire world within 16 days and the images are saved in an archive, so the possibility to find cloud-free images is increasing due to this availability of free data [44]. Each type of satellite images has advantages and disadvantages in detecting windthrows. Malthus et al. [55] have developed a comparative study to emphasize the advantages, limitations and even prices, where possible, of current remote sensing image sources used in *commercial forestry*. Similar comparisons have been developed by Suarez et al. [56], which compared optical techniques with RADAR and LIDAR sensors. Melesse et al. [57] presented the characteristics of 20 different satellite sensors, while [3] summarised the specification of sensors used for *forest disturbance detection*.

The table below (Table 2) summarizes the characteristics of the most important satellite data used in windthrow detection and forest cover monitoring. The most important differences between these data are the spatial resolutions, e.g. from 30 m for Landsat-7 multispectral data to 1 m and even under 1 m for the Ikonos, WorldView, and WuickBird data. But when detecting and assessing windthrows, the choice of the appropriate sensor will depend on the availability of data, cost, scale of the fragmented landscape and area of interest, because the high resolution imagery is not available globally, like Landsat data. If the exact small scale (< 0.5 ha) delineation of the windthrow is needed, then the high-resolution imagery is suitable. But if the goal is to detect large scale windthrows quickly, then the medium resolution data is more useful [44].

Table 2. Characteristics of a number of remote sensing sensors

Sensor	Years	Number of Bands	Multispectral resolution (m)	Panchrom. resolution (m)	Repeat cycle	Scene size (km)	Cost per sq. km

Preprints (www.preprints.org) | NOT PEER-REVIEWED | Posted: 11 September 2017 doi:10.20944/preprints201709.0038.v1

Landsat 4-5 MSS	1982 1999	4	80	—	18days	185 x 185	Free
Landsat 4-5 TM	1982 2012	7	30 120 - thermal	—	16 days	185 x 172	Free
Landsat 7 ETM+	1999	8	30 60 - thermal	15	16 days	185 x 172	Free
Landsat 8	2013	11	30	15	16 days	185 x 180	Free
ASTER	1999	14	15 – band 1-3 30 – band 4-9 90–band10-14	—	1- 2 days	60	Free (on-demand)
MODIS Terra MODIS Aqua	1999 2002	36	250 - 2 bands 500 - 5 bands 1000-29bands	—	1-16 days	2330	Free
SPOT 1-3	1986 1997	3	20	10	26 days	60 x 60	$1,200 per scene
SPOT 4	1998 2013	4	20	10	26 days	60 x 60	$1,200 per scene
SPOT 5	2002	4	10	2.5 / 5	26 days	60 x 60	$2,700 per scene
SPOT 6-7	2012	4	6	1.5	26 days	60 x 60	$5.15
IKONOS	1999	4	4	1	14 days Less than 3 days	11.3	$30- 53 per scene
QuickBird	2001	4	2.4	0.61	Between 1 and 2.8 days	16.8	$18
FORMOSAT 2	2004	5	8	2	daily	24x24	
Pléiades 1A-1B	2011	4	2	0.5	26 days daily	20	$13 - 40
WorldView-1	2007	1	—	0.46	3.7 days (for 0.52 m) 1.1 days (for 1 m)	17.6 x 14	$14 - 48
WorldView-2	2009	8	1.84	0.46	Up to 1.1 days	16.4	$14 - 58
WorldView-3	2014	28	1.24	0.31	between 1 to 4.5 days	13.1	$19
WorldView-4	2016	4	1.24	0.31	less than 3 days	—	—
RapidEye	2008	5	5		between 1 to 5.5 days	25x25	$14 - 55
Sentinel 1A and 1B	2014, 2016	1 SAR band	variable		5 to 12 days	—	free
Sentinel 2A and 2B	2015, 2017	13	variable		5 to 10 days	—	free

* Source [60,61]

** Prices are only estimates based on online sources, and may vary and the price can increase due to the demanding rules set by the providers. E.g. - usually the minimum order area for archive imagery is 25 sq. /km with a 2 km (digital globe) or 3 km (GeoEye) minimum order width.

Preprints (www.preprints.org) | NOT PEER-REVIEWED | Posted: 11 September 2017 doi:10.20944/preprints201709.0038.v1

The free access policy for Landsat data has made this data more and more frequently used in remote sensing studies [60,61]. However, with the accessibility of these data, there is a challenge to find images without clouds or with very little cloud coverage in the analysed area, because clouds can significantly influence the reflection from different spectral bands [62]. This is an issue we have also faced and we will present next how we have solved this shortcoming

4. Materials and Methods

In this study we aimed to highlight the applicability and efficiency of Landsat data in detecting diffuse windthrows caused by the Xhyntia storm that crossed the Vosges Mountains on 28 February 2010. Windthrow detection depends on the affected area. If the affected area is larger, the detection capability increases, together with the results accuracy of the Landsat satellite images based analysis. Figure 3 illustrates the methodological workflow.

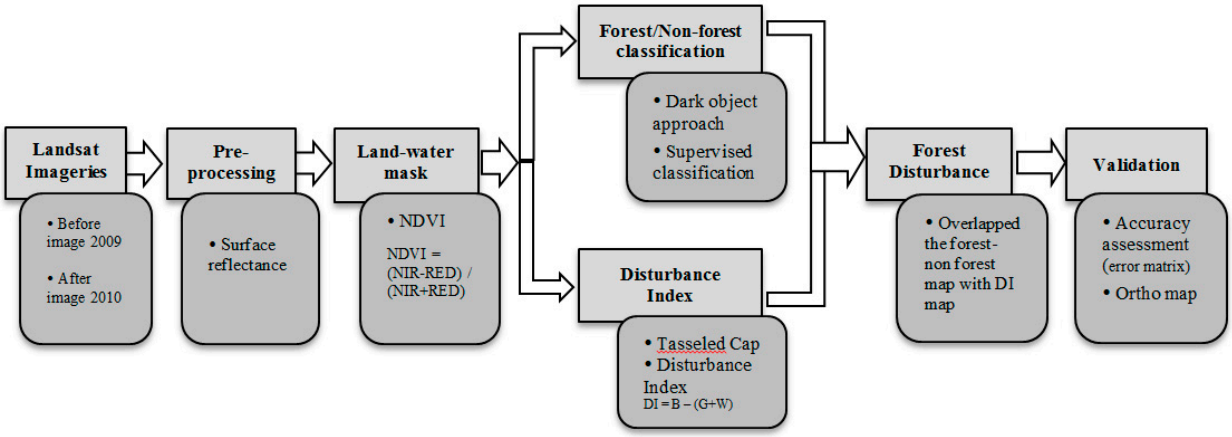

Figure 3. Methodological steps

We started with the pre-processing of satellite imagery, namely converting them from digital numbers into reflectance. The next step consists in masking the water bodies and dark soil to avoid these pixels being confused with pixels corresponding to the vegetation areas, by using the NDVI index values. Then the images were classified into forest and non-forest areas. The classification was made for the two images, before and after the storm, respectively. Then the difference between the classified images was made, resulting into the identification of areas with lost forest vegetation.

In addition, to improve the result obtained in the previous step, the Disturbance Index (DI) was used. The calculation of DI is made based on the Tasselled Cap bands. After overlapping the two resulting images we obtained the forest changes map. Then, the validation of results was carried out. The evaluation of results depends on the data and information used. The accuracy can be directly influenced by the quality and availability of the ground data (the resolution of orthophotos, high-resolution satellite imagery). The first step in results validation is to calculate the accuracy assessment and the Kappa statistic. Another validation was made by overlapping the polygons resulting from the change map with the orthophotos from 2009 and with the RapidEye satellite image from 2010.

4.1. Pre-processing, land-water and cloud mask

Landsat satellite images were used for windthrow detection. The images were purchased for the previous year and the year after the meteorological phenomenon (28 February 2010) that has led to the fall of trees in the Vosges Mountains. Thereby, a multi-temporal set of Landsat 5 TM images (with 7 spectral bands - 30 m spatial resolution) was used. The images were acquired on different days 17.06.2009, before the Xynthia storm, and on 4.06.2010, after the phenomenon. The Landsat images were downloaded freely from the [63] website. Table 3 shows that between the two dates of image selection there were no meteorological events with extreme wind gusts, no storms or tornadoes. Therefore, the data reflected by the two images cannot be artefacts. We selected no clouds or very

Preprints (www.preprints.org) | NOT PEER-REVIEWED | Posted: 11 September 2017 doi:10.20944/preprints201709.0038.v1

few clouds images that were recorded during the growing season and these were purchased for the same vegetation season (June), to reduce the impact of vegetation in different seasons.

Table 3. The characteristics of the images that were used for the Vosges Mountains area

Date of the Xynthia storm	Path/Row	Lat/Long	Previous to Xynthia	After Xynthia
27-28.02.2010	196/026-027	48.9/6.9	17.06.2009	4.06.2010

In order to use the satellite images to detect changes occurring at the ground surface, several steps are required, namely: selecting the images that best fit the intended purpose, orthorectification, georeferencing, various corrections, calculating some indices to enhance the data information [64]. The Landsat satellite images provided by USGS have already been radiometrically and geometrically corrected, but for the proposed operations we needed the values of the reflective satellite images. This operation was done using the formulas given by Chander & Markham [65]. The first step was to pre-process the two sets of images, before and after the storm, by converting the digital numbers into spectral radiance using the equation:

$$L_\lambda = (gain * DN) + bias_\lambda \quad (1)$$

Where:

L_λ - the spectral radiance at the sensor level and referring to the wavelength λ for the specific band;

DN – Digital Number;

gain and *bias* - are specific calibration parameters determined before launch.

For the relatively clear Landsat images, a reduction in variability of images can be made by converting spectral radiance, calculated using equation (1), into surface reflectance or albedo. To obtain surface reflectance, the fraction of solar energy reflected on a certain wavelength, the following equation was used:

$$R_\lambda = (\pi * L_\lambda * d^2) / (ESUN_\lambda * \sin\theta_s) \quad (2)$$

Where:

R_λ - Spectral radiance at the sensor's aperture;

L_λ - Spectral radiance at the sensor's aperture calculated through equation 1;

d - Earth-Sun distance [astronomical units];

$ESUN_\lambda$ - Mean exoatmospheric solar irradiance [66];

$Sin\theta_s$ - solar zenith angle in degrees

The next step consists in masking the clouds, as we mentioned previously. This step is essential because during the detection process, the pixels corresponding to the clouds or their shadows can be confused with darker vegetation pixels, such as the coniferous forests. Clouds are difficult to detect on Landsat images, due to the spectral properties of these images and the complexity of the clouds [67]. It may be more difficult to distinguish the shadow of clouds from "false shades" [64] given by the dark soils, the topographic shadows, water, etc. For example, Huang et al. [26] reported difficulties in separating shadows from the spectral response of waters (cited by [62]). On the other hand, the lack of adequate images may introduce errors in the process of masking the clouds and lead to the inability to differentiate between the cloud shadows and the topographic shadows where there are areas with shadow potential [61,68]. If the areas with changes are relatively small, this error time significantly decreases the detection accuracy of the changes [67]. The clouds and associated shadows were separated through a classification of associated pixels and excluded from the subsequent analyses of the changes occurred in the studied area. After applying this mask, the areas where clouds and shadows were located received the value "No data", not taking into account subsequent processing.

Preprints (www.preprints.org) | NOT PEER-REVIEWED | Posted: 11 September 2017 doi:10.20944/preprints201709.0038.v1

In addition to the masking of clouds and their associated shadows, it is necessary to apply another mask for some non-forest dark surfaces such as water, dark soil, and dark impervious surfaces because these can be as dark as or even darker than forest pixels [26]. To identify and remove these pixels we used the method proposed by Huang et al. [26], which is based on the spectral properties of water bodies and dark soil. Pixels are classified as water or dark soil if they have reduced reflection in the SWIR band and if they have low NDVI index values calculated based on the RED and NIR reflectance bands:

$$NDVI = (NIR-RED)/(NIR+RED) \quad (3)$$

After calculating the Normalized Vegetation Difference Index, a threshold was set to delineate the land-cover classes from the masked areas covered by water and soil, respectively. In this study the threshold 0.25 was used. To exemplify the result we performed a zoom on a 26.6 km x 20.5 km sample area, i.e. on a 54,613 ha area, which has the Remiremont city in the centre (Figure 4), a sample that was also used for the other examples. This step made it possible to identify and eliminate pixels that may be problematic throughout the next steps.

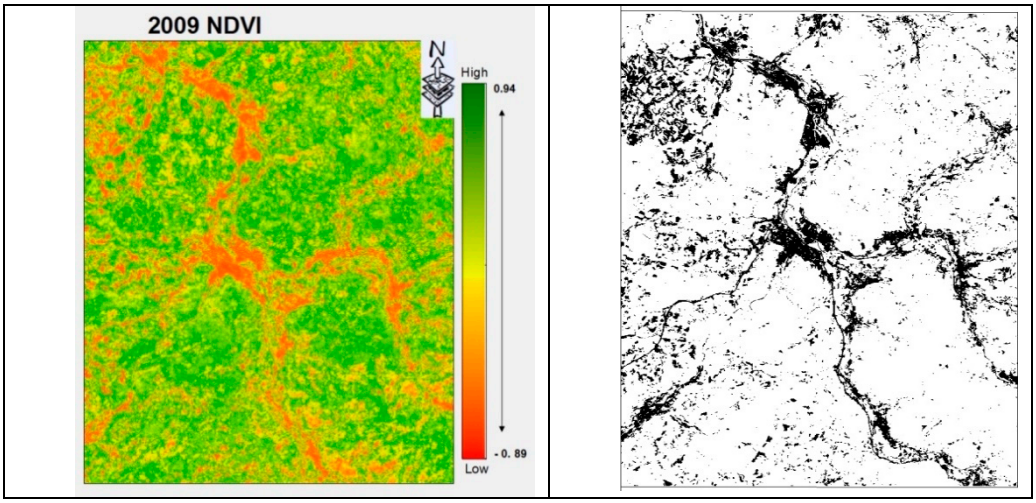

Figure 4. NDVI values (a) and masking of non-vegetated dark objects (b)

4.2. Training and image classification

In order to obtain the forest areas, the image before the Xynthia storm must be classified into "forest" and "non-forest". This is carried out following two steps: automatic extraction of forest pixels based on the histogram, and by conducting a supervised classification of the two images before and after the occurrence of the phenomenon.

4.2.1. Automatic extraction of forest pixels

The forest pixels have been identified using the "dark object" approach [30] which involves the delineation of the "forest peak", based on a band local histogram (Figure 5). In the absence of non-vegetated dark objects (which were masked previously), the forest pixels will be located to the left of the histogram, while the first peak on the left will be considered the "peak forest".

Huang et al. [30] recommends taking into account two major factors:

i) delineation should be done for a local image window, because this area will contain fewer classes of land cover and the delineation of forest classes from other classes will be easier to achieve.

ii) selection should be made of the appropriate band to create the histogram which sets the basis for class delineation.

Preprints (www.preprints.org) | NOT PEER-REVIEWED | Posted: 11 September 2017 doi:10.20944/preprints201709.0038.v1

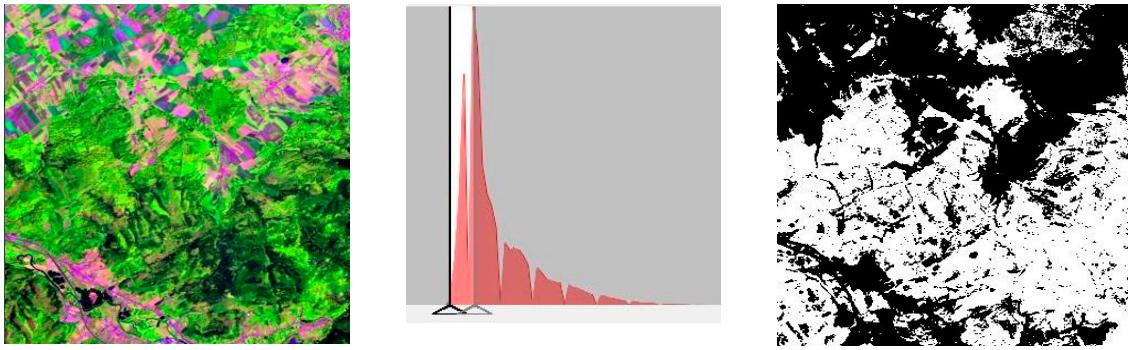

a) satellite image in 5-4-3 combination

b) delineation of "forest peak" using RED band histogram

c) forest pixels (white) after applying the 0.25 threshold

Figure 5. The procedure for the delineation of forest pixels based on the histogram for the local image window, (adapted after Huang et al. [30])

In order to determine whether pixels have been classified properly into forest and non-forest, we have set samples of black pixels representing vegetation based on which we calculated the Integrated Forest Index (IFI) [24, 30].

$$IFI = \sqrt{\frac{1}{NB}\sum_{i=1}^{NB}\left(\frac{b_{pi}-\bar{b}_i}{SD_i}\right)^2} \quad (4)$$

where:

$\bar{b}_i$ and SD_i are the mean and standard deviation of forest training pixels within the image for band *I;*

b_{pi} is the band *i* spectral value for pixel *p;*

NB is the number of spectral bands.

Low IFIs values indicate a high probability of wooded areas, while high values indicate high probability of other land cover categories. Certain dark pixels corresponding to crops may be spectrally similar to pixels for forest areas, but will have IFIs values lower than the forest areas. To eliminate them, it is necessary to set a threshold value, which separates the forest areas from the other areas. For the present study, the threshold was set to 3, so pixels smaller than or equal to 3 are considered as belonging to the wooded areas.

4.2.2. Supervised classification

The general objective of the image classification procedure is to classify all the pixels from an image in classes of ground cover or themes. The purpose of the classification in this study is to complement the result of extracting forest pixels by means of the histogram. First of all, land cover classes (water bodies), forest areas (conifers, mixed and deciduous trees), urban areas, pastures and agricultural areas were established and the pixels were selected for the classification algorithm to acknowledge the classes. After running the classification algorithm (Figure 6a), the resulting images have been reclassified into forest areas and non-forest areas. Finally, following the classification of both images from 2009 and 2010, the separation of the forest areas from the non-forest areas was achieved (Figure 6b). This will be used in the end to obtain a change map for the two analysed temporal frames.

Preprints (www.preprints.org) | NOT PEER-REVIEWED | Posted: 11 September 2017 doi:10.20944/preprints201709.0038.v1

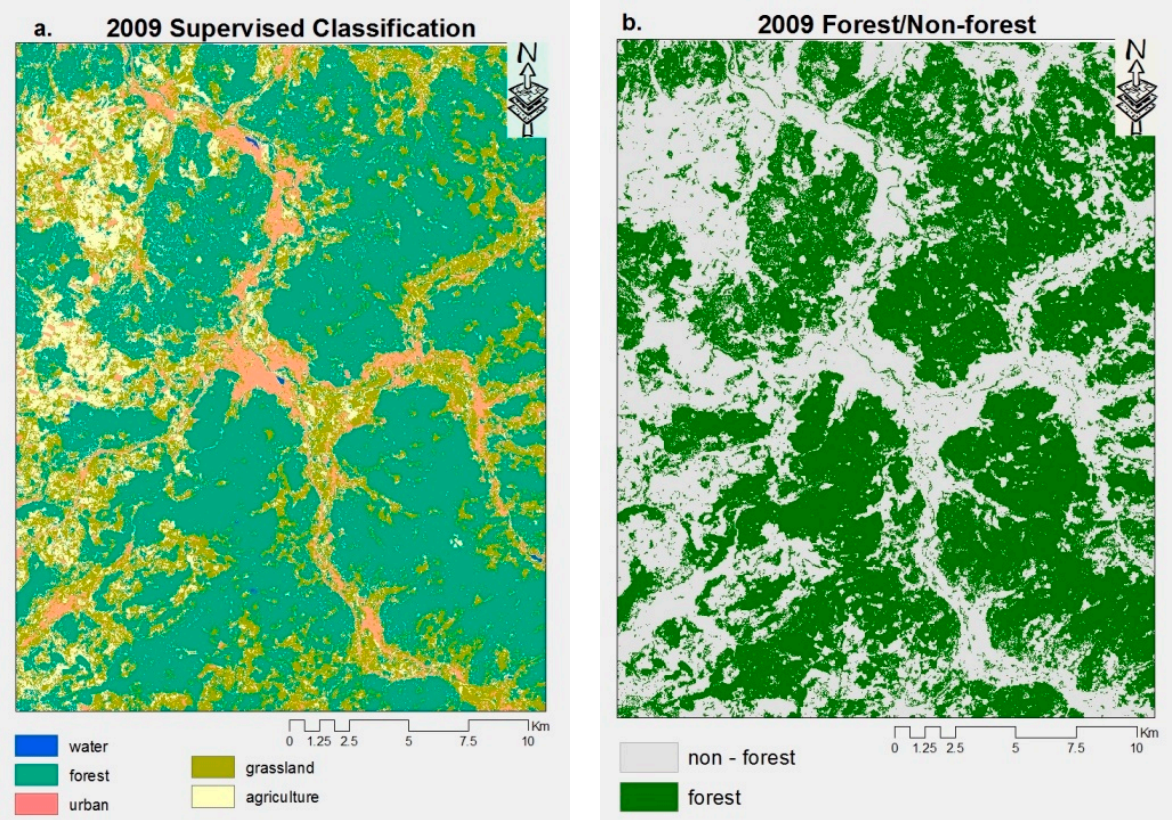

Figure 6. Supervised classification (a) and forest/non-forest classification (b).

4.3. Forest Disturbance Detection

The detection of forest disturbed areas was carried out using the Disturbance Index (DI) developed by Healey et al. [23] and applied by [24, 69-75]. DI was developed to highlight the spectral signatures of non-vegetated areas associated with disturbance zones and to separate them from all other spectral signatures of the forest areas. The procedure is based on a combination of bands resulting from the Tasselled Cap Transformation, which reduces the six bands of Landsat TM image (excluding the thermal band) into three bands that render brightness, greenness, and wetness.

This index highlights the difference in spectral signatures and thus disturbed forest areas have higher brightness values and lower values for greenness and wetness bands compared to undisturbed forest areas. The index is calculated based on the formula:

$$DI = Br - (Gr + Wr) \quad (5)$$

Where: Br, Gr, Wr are the Tasselled Cap bands, standardized (resized) around the scene's mean forest value.

The result of the calculation is a single band, where positive values generally indicate areas with disturbance. In order to separate the disturbed areas from the non-disturbed ones, it is necessary to identify a limit threshold, depending on the environmental conditions in the studied area. In our case, the value of DI = 2.5 best identifies the areas affected by windthrows.

The last step involved the overlapping of the initial image classified as “forest areas” and “non-forest areas” with the map derived from the DI calculation, and so we obtained a change map for the forest area in the Vosges Mountains in 2009-2010 (Figure 7).

Preprints (www.preprints.org) | NOT PEER-REVIEWED | Posted: 11 September 2017 doi:10.20944/preprints201709.0038.v1

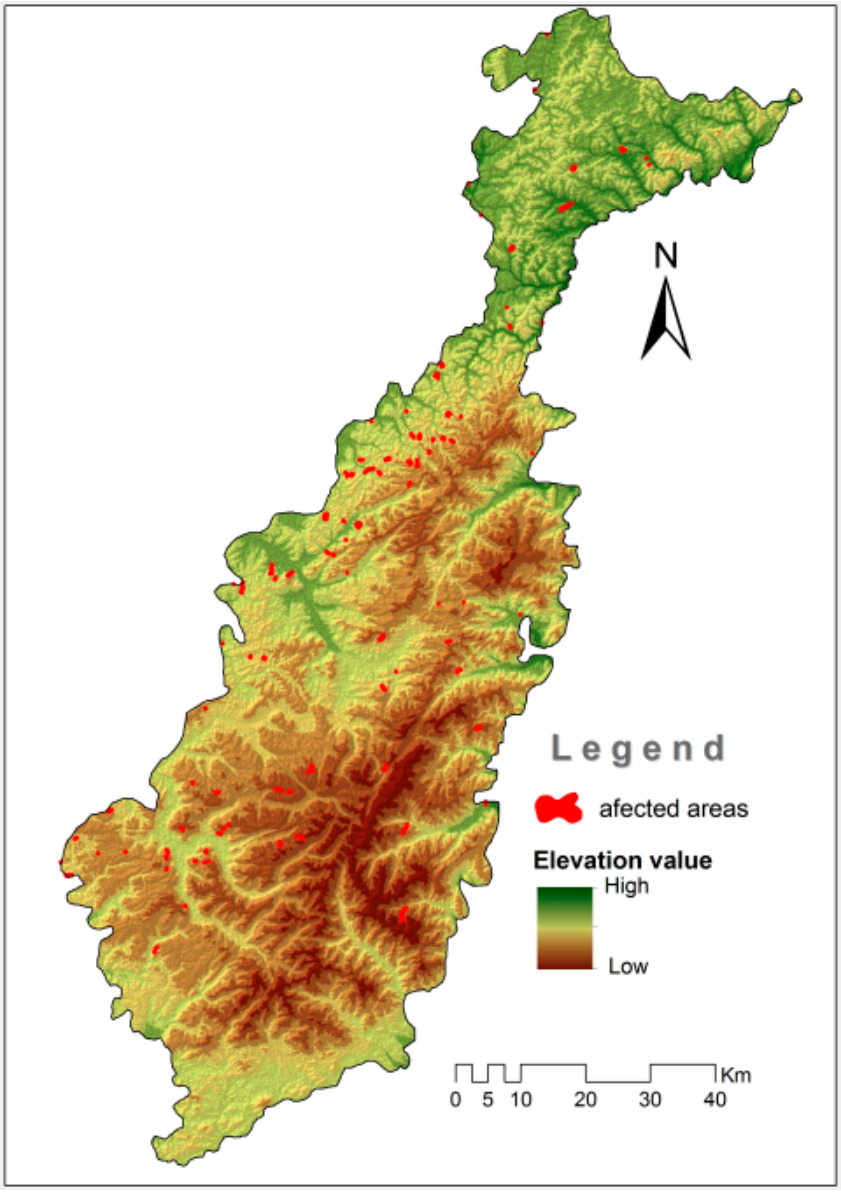

Figure 7. Areas affected by diffuse windthrow.

As seen in Figure 7, diffuse windthrows occur in the form of scattered polygons, or rather points, on the territory of the Vosges Mountains, some points being so small that they cannot be visually perceived at the scale of cartographic representation in the figure above. We identified 257 polygons (list available in Table S1: Polygons obtained after running the detection algorithm), affected by windthrows, with a total area of 229 ha. We attach additional material to indicate diffuse windthrow (Appendix A).

5. Results and discussions

In the algorithm we have developed, we included neither the object-based image analysis nor the segmentation procedures. We will explain next why we particularly made this decision. Segmentation techniques are recommended to detect possible changes, especially for high-resolution satellite imagery. Comparing the results obtained by the segmentation of the Landsat images with high-resolution images, it was revealed that Landsat results provide a low accuracy [76]. The classes are not well defined. The analysis is more difficult and requires a high user experience [77]. In addition to the resolution characteristics, there are other factors such as geomorphological structure, topography, and dead vegetation [78], that affect the applicability of segmentation on Landsat

 doi:10.20944/preprints201709.0038.v1

images. The algorithm we propose is similar to the French methodology known as the "7-point method" [33]. However, this still includes different stages, proving to be effective in detecting diffuse windthrows based on Landsat images.

The difference between this method and the "7 points" method is given by the steps followed and the approaches used. The first difference is given by the satellite images used. This study is based on medium-resolution Landsat satellite images, while the "7 points" method uses high resolution images. In the "7 points" method, "pixel per pixel" is used in order to detect the changes. The same "pixel per pixel" approach was also used in this study, but it was applied to forest/non-forest images. The next stage in the "7 points" approach consisted in the segmentation of the disturbed areas. As Darwish et al. [76] stated, the segmentation techniques on the Landsat images emphasized the fact that the results provided a low accuracy. Therefore, this method is not recommended for medium resolution images. Instead, in this study we used the Disturbance Index to detect the affected areas. This index is calculated based on the bands obtained from the Tasselled Cap Transformation and it highlights the difference in spectral signatures. Thereby, the disturbed forest areas have higher brightness values and lower greenness and wetness values compared to undisturbed forest areas.

The last step in the "7 points method" is to integrate the results obtained by segmentation with the soil results. Thus, by classifying the disturbances produced, a map of damages was obtained. Due to lack of ground data, we have chosen to do a validation based on the error matrix. Thus, we have calculated the accuracy for the supervised classification into forest and non-forest categories, as well as for the map of changes in forest areas. This map was obtained by overlaying the two resulting maps (from the difference between the forest/non-forest image and the image resulting from the DI calculation). For validation, we overlapped the resulting polygons from change map on the 2009 orthophotos and the 2010 RapidEye satellite image (Figure 9).

5.1. Accuracy Assessment

To evaluate the quality of the analysis, we assessed the overall accuracy and the Kappa coefficient. Following the classification of the two images, the accuracy assessment was performed in two steps: a) the accuracy of supervised classification and of forest/non-forest classification and b) the accuracy of the forest change map.

To evaluate the accuracy of the supervised classification, we used 100 random points for each class we used. These points were manually labelled using Quickbird Google Earth and RapidEye high-resolution imagery [79]. These high-resolution images were used only for the confirmation and validation of the classification. Also, for results verification and validation purposes, orthophotoplans from 2009 were used, with a resolution of 2.5 and 5 m, available on [80].

The polygons resulting from the detection process were overlapped with the ortophotos to see whether there is vegetation in the detected areas. The result was summarized in an error matrix, while calculating the overall accuracy and the Kappa coefficient. Therefore, the accuracy assessment calculated for the forest/non-forest classification is given by the overall accuracy = 94.14% and by the Kappa coefficient = 0.92. The evaluation of the forest changes occurred between 2009 and 2010 was carried out based on a sample of 300 points. The previously defined samples considered as real elements in the field were used to calculate the error matrix, the overall accuracy, the kappa statistic and the user's and producer's accuracy for each class, as shown in Table 4.

For the change map we used three classes, namely *constant forest* (CF) that did not change in the two images, *disturbed areas* (D) and *other non-forest classes* (NF). The constant forest area is given by those areas that were represented by forest both in the *before Xynthia* storm image and in the *after Xynthia* image, while the areas with disturbances are those areas that were classified as forest in the *before Xynthia* image and that appeared as non-forest in the *after Xynthia* image. The overall accuracy obtained for the change map was high, i.e. 86%, and the value of the Kappa coefficient was 0.84. Also, the class represented by the constant forest had the user's and producer's accuracy higher than the disturbance class.

Table 4. The accuracy assessment calculated for the change map

 doi:10.20944/preprints201709.0038.v1

(CF=constant forest class; D=disturbance class; CNF=constant non-forest class)

Overall accuracy (%)	Kappa statistic	User's accuracy (%)			Producer's accuracy (%)		
		CF	D	CNF	CF	D	CNF
86	0.84	89.10	78	88	81	80	88.47

5.2. Results validation

Once the accuracy of the thematic data has been set, the validation of the results was the next step. Detecting forest surface changes using satellite imagery is a difficult task and requires validation using ground data. The validation was conducted based on disturbance data occurred in 2010 in the mountains area (data available on [81], referring to all types of disturbances, not only windthrows), on the cadastral forest plots for the two years (data available on [82], as well as on the orthophotos of 2009 and the high-resolution satellite imagery of 2010. For the final validation we used the change map obtained previously and we combined it with data on disturbed forest areas, according to the French National Forest Inventory (IFN). The resulting polygons during the detection process were overlapped with the disturbed areas. Hence, we obtained a first validation of the results. Figure 8 highlights one of the polygons detected from the image processing, overlapped with the Landsat satellite image of 2009 (Figure 8b), and the Landsat image in 2010, respectively (Figure 8c).

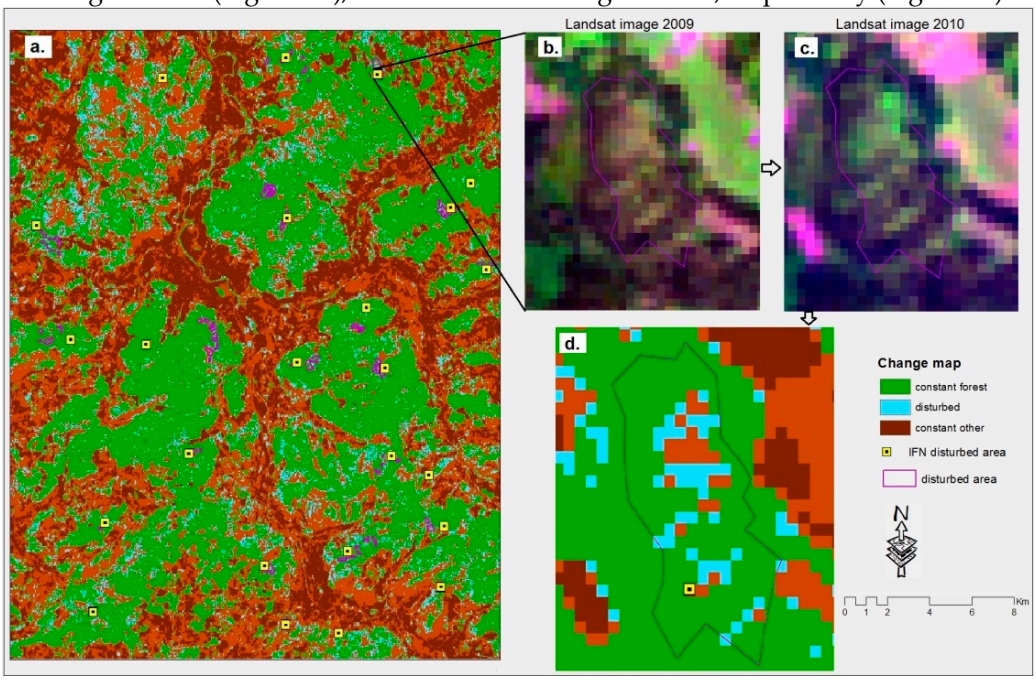

Figure 8. Forest change map **(a)** overlapped with the polygons resulting from the detection process, as well as the points where windthrows occurred in 2010 (according to INF): one polygon overlapped with the 2009 satellite image **(b),** and the 2010, respectively **(c)**, and a zoom on the same polygon **(d)**.

Also, in order to obtain a picture of the "ground-truth", this polygon was overlapped with the orthophoto of 2009, and with the 2010 RapidEye high-resolution image (Figure 9), thus achieving a new validation.

 doi:10.20944/preprints201709.0038.v1

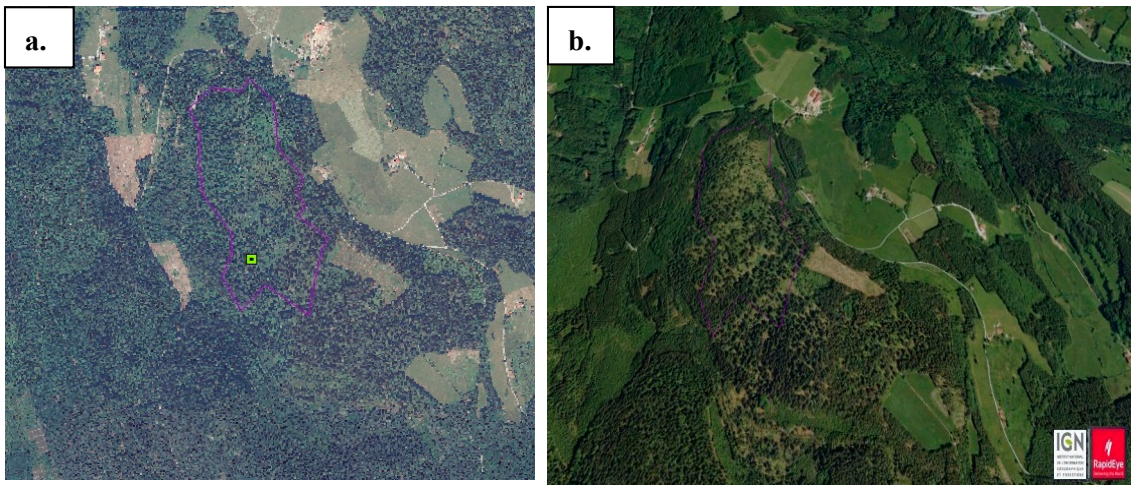

523 **Figure 9**. Overlapping a polygon extracted through the detection process with the 2009
524 orthophoto (a) and with the satellite image in 2010 (b).

525 Another validation was carried out using high-resolution satellite imagery available in Google
526 Earth. For an easier interpretation of the effect of the Xynthia storm, we zoomed out to a sample
527 territory of 26.6 km x 20.5 km, i.e. 54,613 ha, which is in the centre of the Remiremont city (Figure 10).
528 Hence, Figure 10(b) highlights another polygon obtained as a result of the disturbed areas
529 detection process. This polygon is superimposed on the change map (in raster format). In the
530 windthrows detection phase, raster data were used which were subsequently converted into vector
531 data in order to overlap the final results. By converting these images, a comparison between the
532 results detected on raster format (blue colour) and vector representation (purple polygon) was
533 achieved. The geometric effect of this polygon obtained by switching from raster format to vector
534 format suggests a possible underestimation of the actual area damaged by the wind. Figure 10 (d)
535 shows the image *before* the Xhyntia storm, while Figure 10 (c) illustrates the forest state *after* the
536 Xhyntia storm.
537

Preprints (www.preprints.org) | NOT PEER-REVIEWED | Posted: 11 September 2017 doi:10.20944/preprints201709.0038.v1

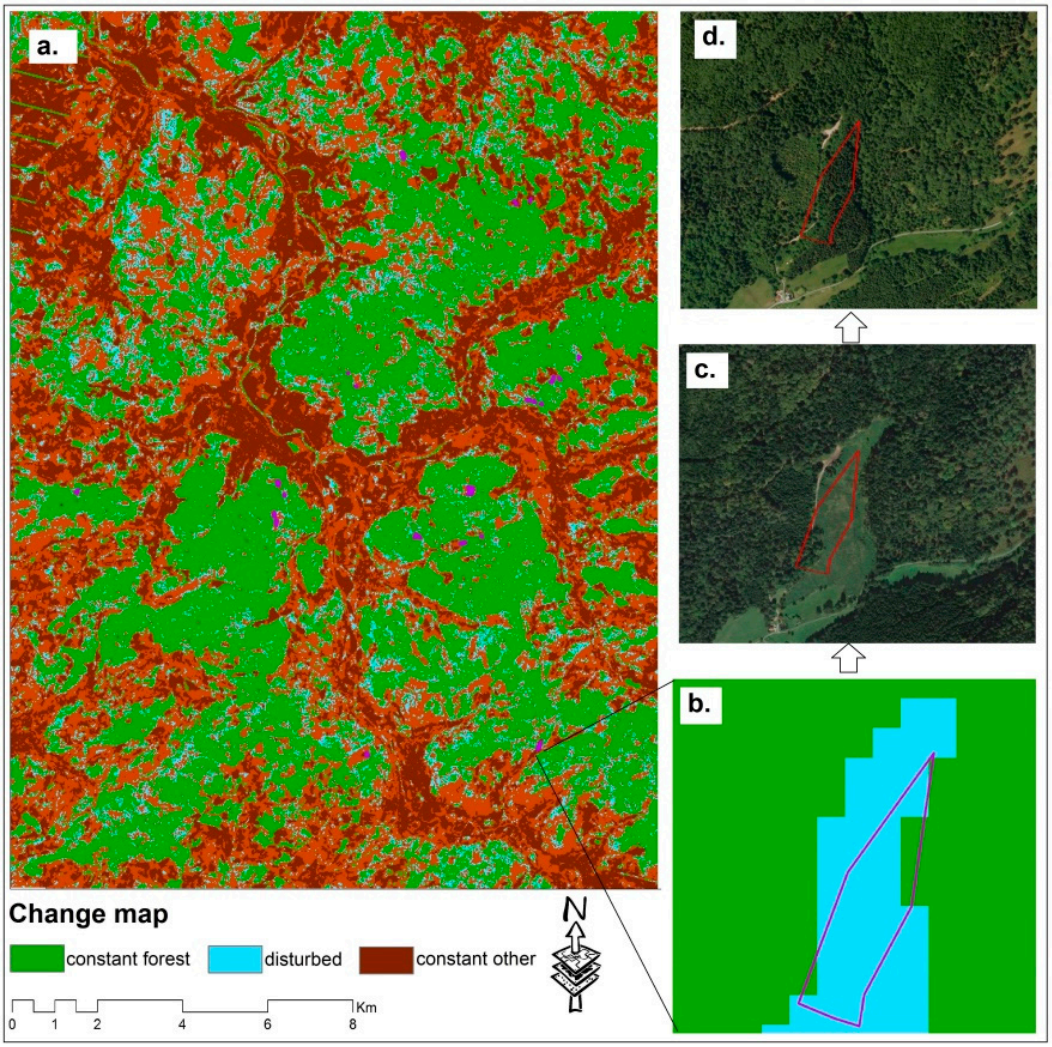

Figure 10. The forest change map overlaid with the polygons resulting from the detection process **(a);** zooming one polygon (b); the same polygon overlapped with the 2009 Goggle Earth satellite image **(c)** and from 2010, respectively **(d)**

5. Conclusions

The tree windthrows caused by storms are much easier to detect by the authorities if they are contiguous, compared to the diffuse or isolated ones. The diffuse windthrows occur in the temperate zone at wind gusts of 100-140 km/h and their areas range between a few tens of square meters and a few hectares, but they are very numerous, of several hundreds in the wooded mountain massifs. For this reason, they are more difficult to detect, map and, obviously, it is much more difficult to characterize the extent of the damage. However, the detection of changes occurred as a result of the diffuse windthrows, even if they are several hundred, is also important in order to set the spatial and temporal rehabilitation and forest management trends. In this regard, this paper presents a rapid procedure for the detection of the diffuse windthrows based on low cost images, knowing that certain sensors cannot be accessed without significant investments. Our application is based on the study of effects caused by the Xynthia storm in the Vosges Mountains, on 28 February 2010.

The results of this research highlight the usefulness of the Landsat satellite imagery, more easily to access than other types of images for the analysis and detection of windthrows. The detection of areas damaged by the Xynthia storm by applying the pixels delineation method based on the histogram enabled us to automatically delimit the forest pixels from the non-forest ones, thus reducing the working time. The Disturbance Index enabled the more accurate delineation of the affected areas.

The classification of the area into forest and non-forest increases the precision level for the detection of affected areas. The Tasseled Cap Transformation and the calculation of the Disturbance Index enable us to highlight the affected areas. The accuracy assessment of the results obtained for the change map was high (86 % overall accuracy and the value of the Kappa coefficient was 0.84). Also, the constant forest class in the two images, before and after the phenomenon, had the user's and producer's accuracy higher than the disturbance class, i.e. 89.10% and 81% respectively, compared to 78% and 80%.

The spatial analysis enabled us to highlight the most affected areas, resulting in 257 affected polygons, totalling 229 ha. The largest polygon is 13 ha, located east from the Grand-Soldat hamlet, Abreschviller village, department of Moselle. Moreover, following the analysis conducted, it was concluded that most of the affected polygons had a predominantly coniferous vegetation composition (75%), with slopes facing N, NW and W. For validation purposes, high-resolution images and orthophotoplans taken before and after the storm were used. The error matrix was calculated, achieving an overall accuracy of 86%, which reveals that our methodology adapted for low cost image resources, can be used for the rapid detection of diffuse windthrows in the temperate zone.

Supplementary Materials:

Table S1. Polygons obtained after running the detection algorithm.

Acknowledgments: This research was supported by Centre de recherche en Géographie, LOTTER-EA7304, Université de Lorraine, Metz. The second author mentions that his contribution is a product of the activity undertaken in 2015 at the Laboratory LOTERR-EA7304 during the Erasmus scholarship mobility.

Author Contributions: I. Haidu and P. Furtuna conceived and designed the experiments; P. Furtuna performed the experiments; I. Haidu and S. Lébaut analyzed the data; P. Furtuna, I.Haidu and S. Lébaut wrote the paper.

Conflicts of Interest: The authors declare no conflict of interest.

Appendix A

The largest polygon has an area of 13 ha (450-550 m altitude), East of the Grand-Soldat hamlet, Abreschviller village, department of Moselle. In the neighbouring Southern village of Saint-Quirin, the second disturbed polygon is the size of 9.2 ha (450-330 m altitude). Also in Moselle there is a 7.7 ha polygon in the Northern Vosges Regional Natural Park, North of Baerenthal and a 7.9 hectare polygon South-West of Mouterhouse. In the department of Vosges there is a 6.1 hectare polygon South of Arrentès-de-Corcieux. In the department of Haut-Rhin in Alsace there is a 7.5 ha disturbed area North-West of Lake Grand Ballon, on the territory of the Lauteenbach-Zell village.

Following the conducted analysis, it was found that most of the affected polygons had predominantly coniferous vegetation (75%), at an average altitude of 950 m, with N-, NW- and W-facing slopes. Of the 257 polygons, only 7 have more than 5 hectares of disturbed area, but they are 51.12 % of the total windthrow area. 56 polygons range from 1 to 5 ha and the remaining 194 polygons are under 1 ha. The smallest affected polygon detected by the methodology presented above and based on the limited data images approach is 0.09 ha. This is much better than the detection threshold based on 1 ha of satellite imagery that was used to assess the damages caused by the 1999 storms [83].

The large number of small polygons detected, 194 polygons under 1 ha, come as a result of the particularities of interaction between high wind speeds, over 130 km/h and the relief features of the Vosges Mountains. Generally, the affected polygons appear on the slopes facing the direction of the Xynthia storm. At the escalation of the slopes, the speed of the wind gusts accelerated resulting in an effect similar to bearing, resulting in a greater pressure exerted on the forest cover area.

References

1. Rauch, E. Wind and storms. In: Pfister, C., Schellnhuber, H., Rahmstorf, S., Graßl, H. (Eds.), Weather catastrophies and climate change. Is there still hope for us? MunichRe, Munich, **2005**, pp. 132–143.

2. Bernardes, S.; Madden, M. (2016) Vegetation disturbance and recovery following a rare windthrow event in the Great Smoky Mountains National Park, Int. Arch. *Photogramm. Remote Sens. Spatial Inf. Sci.*, XLI-B8, **2016**, pp.571-575. DOI:10.5194/isprs-archives-XLI-B8-571-2016
3. Einzmann K.; Immitzer M.; Böck S.; Bauer O.; Schmitt, A.; Atzberger, A. Windthrow Detection in European Forests with Very High-Resolution Optical Data. Forests, **2017**, 8, 21, DOI10.3390/f8010021.
4. Vernier, F. L'ouragan Lothar, 26 décembre 1999 effets et perspectives sur la forêt Lorraine. Bulletin de l'Académie Lorraine des Sciences, **2001**, 40 (1-2), 40-50.
5. Birot, Y. ; Landmann, G.; Bonhême, I. *La forêt face aux tempêtes*. Editeur: Quae, France **2009**, ISBN 978-2-7592-0330-7
6. Inventaire Forestier National - IFN Tempête Klaus du 24 janvier 2009: 234 000 hectares de forêt affectés à plus de 40 % 42,5 millions de mètres cubes de dégât. L'IF, **2009**, nr. 21, 1er trimestre. Available online http://inventaire-forestier.ign.fr/spip/IMG/pdf/IF21_internet.pdf.
7. Pôle interrégional de la Santé des Forêts du Nord-Est. *Bilan de la santé des forets 2010 en Alsace*. DRAAF/SRAL, Département de la santé des forêts, Metz, **2011**a.
8. Pôle interrégional de la Santé des Forêts du Nord-Est. *Bilan de la santé des forets 2010 en Lorraine.* DRAAF/SRAL, Département de la santé des forêts, Metz, **2011**b.
9. Anziani, A. Rapport d'information sur les conséquences de la tempête Xynthia. Session ordinaire du Sénat, **2010**, No. 554/10 juin, 100p.
10. Hernu, H.; Kbaier, R.; Rochard, J.; Casteigts, M.; Furst, X.; Jullien, B.; Balay, L.P.; Guillet, M. Rapport sur l'évaluation des dommages causés par la tempête xvnthia des 27 et 28 févri er 2010 à prendre en compte a titre du fonds de s olidarité de l'union européenne Ministère de l'écologie, de l'énergie, du développement durable et de la mer, **2010**.
11. FFSA/GEMA, Fédération française des sociétés d'assurances / Groupement des entreprises mutuelles d'assurance. La tempête Xynthia du 28 février 2010 – Bilan chiffré au 31 décembre 2010. **2011**, 21 pp.
12. Calvet, M.M.; Manable, C. Rapport d'information sur *Xynthia 5 ans après: pour une véritable culture du risque dans les territoires*. Session ordinaire du Sénat, **2015**, No. 536/18 juin.
13. Office national des forêts - *Tempête Xynthia: des dégâts diffus en forêt*, **2010**. Available online: http://www.foretpriveefrancaise.com/actualite/voir/515/page:24. Accessed: 12 July, 2016.
14. Forêt Privée Française (FPF). Available online http://www.foretpriveefrancaise.com/tempete-xynthia-des-degats-localise
15. Papaik, M.J; Canham, C.D. Species resistance and community response to wind disturbance regimes in northern temperate forests. *J Ecol*, **2006**, 94:1011–1026.
16. Bonan, G.B. Forests and climate change: forcings, feedbacks, and the climate benefits of forests. *Science*, **2008,** 320(5882) pp.1444-9. DOI: 10.1126/science.1155121.
17. Klaus, M.;, Holsten, A.; Hostert, P.; Kropp, J. P. (2011) Integrated methodology to assess windthrow impacts on forest stands under climate change. *Forest Ecology and Management*,**2011**, 261, pp.1799-1810.
18. Merry, K.; Bettinger, P.; Hepinstall-Cymerman, J. A prototype model for estimating the location of forest damage from tropical cyclones. *Geographia Technica*, **2011**, 6, 2, pp.65-80.
19. Thom, D.; Rammer, W.; Dirnböck, T.; Müller, J.; Kobler, J.; Katzensteiner, K.; Helm, N.; Seidl, R. The impacts of climate change and disturbance on spatio-temporal trajectories of biodiversity in a temperate forest landscape. *J Appl Ecol*, **2017**, 54, pp. 28–38.
20. Seidl, R.; Schelhaas, M.J.; Rammer, W.; Verkerk, P.J. Increasing forest disturbances in Europe and their impact on carbon storage. *Nat Clim Chang*, **2014**, 4 (9), p. 806–810
21. Merry, K.; Bettinger, P.; Siry, J.; Bowker, J.M. (2015) Estimating urban forest carbon sequestration potential in the southern United States using current remote sensing imagery sources. *Geographia Technica*, **2015**, 10, 2, pp.78-89.
22. Huang, C.; Wylie, B.; Yang, L.; Homer, C.; Zylstra, G. Derivation of a tasselled cap transformation based on Landsat 7 at-satellite reflectance. *Int. J. Remote Sensing*, **2002,** 23, 8, pp.1741-1748. DOI: 10.1080/01431160110106113
23. Healey, S.P.; Cohen, W.B.; Zhiqiang, Y.; Krankina, O.N. Comparison of Tasseled Cap-based Landsat data structures for use in forest disturbance detection. *Remote Sens. Environ.*, **2005**, 97, pp.301–310. DOI: 10.1016/j.rse.2005.05.009

24. Baumann, M.; Ozdogan, M.; Wolter, P.T.; Krylov, A.; Vladimirova, N.; Radeloff, V.C. (2014), Landsat remote sensing of forest windfall disturbance. *Remote Sens. Environ.*, **2014**,143, pp.171–179. DOI 10.1016/j.rse.2013.12.020.
25. Jin, S.; Sader, S.A. Comparison of time-series tasseled cap wetness and the normalized difference moisture index in detecting forest disturbances. *Remote Sens. Environ*. **2005,** 94(3) pp.364-372. DOI: 10.1016/j.rse.2004.10. 012
26. Huang, C.; Goward, S.N.; Masek, J.G.; Thomas, N.; Zhu, Z.; Vogelmann, J.E. An automated approach for reconstructing recent forest disturbance history using dense Landsat time series stacks. *Remote Sens. Environ.*, **2010**, 114, pp.183–198. DOI: 10.1016/j.rse.2007.07.023
27. Zhu, Z.; Woodcock, C.E.; Olofsson, P. Continuous monitoring of forest disturbance using all available Landsat imagery. *Remote Sens. Environ.*, **2012**, 122, pp.75–91.
28. Lambert, J.; Drenou, C.; Denux, J.P.; Balent, G.; Cheret, V. (2013) Monitoring forest decline through remote sensing time series analysis. *GIScience & Remote Sensing*, 2013, 50 (4), pp. 437-457.
29. Stach, N.; Deshayes, M.; Le Toan, T. Mapping storm damage to forests using optical and radar remote sensing – The case of the December 1999 storms in France, in: Olsson H. (Ed.), Proceedings of ForestSat, 2005, Borås May 31–Jun
30. Huang, C.Q.; Song, K.; Kim, S.; Townshend, J.R.G., Davis, P., Masek, J.G., Goward, S.N. Use of a dark object concept and support vector machines to automate forest cover change analysis. *Remote Sens. Environ.*, **2008**, 112, pp.970–985. DOI: 10.1016/j.rse.2007.07.023
31. Kennedy, R.E.; Yang, Z.; Cohen, E.; Braaten, J.; Nelson, P., Spatial and temporal patterns of forest disturbance and regrowth within the area of the Northwest Forest Plan. *Remote Sens. Environ*. **2012,** 122, 117–133
32. Stach, N.; Deshayes, M.; Le Toan, T. Évaluation des dégâts de tempête par télédétection satellitaire: Aspects méthodologiques et opérationnels. Rapport final, Convention DERF Nr. 2001-12-132, 2002, 148.
33. Inventaire Forestier National - IFN (2008), Cartographie des coupes rases des peuplements de pin maritime en Aquitaine par détection satellitaire. Comité interprofessionnel des bois d'Aquitaine (CIBA) et Inventaire Forestier National (IFN), février 2008.
34. Chéret, V. ; Denux, J.P. ; Gacherieu, C. ; Ortisset, J.P. Utilisation de séries temporelles d'images satellitales pour cartographier le dépérissement des boisements résineux du Sud Massif Central. *Rendez-vous Techniques de l'ONF,* **2010**, (31), pp.55-62. http://prodinra.inra.fr/record/179412
35. Hussain, M.; Chen, D.; Cheng, A.; Wei, H.; Stanley, D. Change detection from remotely sensed images: From pixel-based to object-based approaches, *IPRS Journal of Photogrammetry and Remote Sensing*, **2013**, 80**,** 91-106.
36. Sélection Vosges. Available online. http://www.selection-vosges.com/fr/la-foret-vosgienne.html.
37. Garnier, E. Les forêts vosgiennes à l'épreuve des tempêtes sous l'Ancien Régime (XVIIe et XVIIIe siècles). *Revue Gògraphique de l'Est*, **2000**, 40 (3), pp. 1-12.
38. Doll, D. Statistiques historiques des grands chablis éoliens en Europe occidentale depuis le milieu du XIXe siècle: analyse critique. In: Drouineau S., Laroussinie O., Birot Y., Terrasson D., Formery T., Roman-Amat B. *Expertise collective sur les tempêtes, la sensibilité des forêts et sur leur reconstitution*. Dossier de l'environnement de l'INRA n°20, INRA-ME&S, Paris, 2000, pp. 38-41
39. Meteo France. Available online: http://tempetes.meteo.fr/Classification-des-tempetes.html
40. Bedacht, E.; Hofherr ,T. *Winter Storm Xynthia in southwest Europe and Germany*, MUNICH RE Topics Geo, 2010, pp.18-21.
41. Doll, D. Les cataclysmes éoliens dans les forêts d'Europe, aperçu historique. *Forêt Entreprise*, **1991**, 77(5).
42. Dreveton, C. L'évolution du nombre de tempêtes en France sur la période 1950-1999. *La Météorologie,* **2002**, 37, pp. 46-56.
43. Bock, J. ; Vinkler, I. ; Duplat, P. ; Renaud, J.P. Stabilité au vent des hêtraies: les enseignements de la tempête de 1999. Dossier Facteurs de stabilité des peuplements. *Forêt Entreprise*, **2004**, 156, pp. 34-38.
44. Schwarz, M.; Steinmeier, C.; Holecz, F.; Stebler, O.; Wagner, H. Detection of Windthrow in Mountainous Regions with Different Remote Sensing Data and Classification Methods. *Scandinavian Journal of Forest Research*, **2003**, 18:6, pp.525 — 536.
45. Boyle, S.A.; Kennedy, C.M.; Torres. J.; Colman, K., Perez-Estigarribia, P.E.; Sancha, N.U. High-Resolution Satellite Imagery Is an Important yet Underutilized Resource in Conservation Biology. *PLoS ONE,* **2014,** 9(1). DOI:10.1371/journal.pone.0086908.

46. Goward, S.; Arvidson, T.; Williams, D.; Faundeen, J.; Irons, J.; Franks, F. Historical Record of Landsat Global Coverage: Mission Operations, NSLRSDA, and International Cooperator Stations. *Photogrammetric Engineering & Remote Sensing*, **2006,** 72, 10, 1155-1169.
47. Vogelmann, J. E., Gallant, A. L., Shi, H. and Zhu, Z. (2016) Perspectives on monitoring gradual change across the continuity of Landsat sensors using time-series data. *Remote Sens. Environ.*, 185, pp. 258–270
48. Turner, W.; Rondinini, C.; Pettorelli, N.; Mora, B.; Leidner, A.K.; Szantoi, Z.; Buchanan, G.; Dech, S.; Dwyer, J.; Herold, M.; Koh, L.P.; Leimgruber, P.; Taubenboeck, H.; Wegmann, M.; Wikelski, M.; Woodcock, C. Free and open-access satellite data are key to biodiversity conservation. *Biological Conservation*, **2015**, 182, pp. 173–176.
49. Cohen, W.; and Goward, S. Landsat's Role in Ecological Applications of Remote Sensing. *BioScience* **2004**, 54(6), pp535-545. DOI: 10.1641/0006-3568(2004)054[0535:LRIEAO]2.0.CO;2.
50. Mukai, Y.; Hasegawa, I. Extraction of damaged areas of windfall trees by typhoons using Landsat TM data. *International Journal of Remote Sensing*, *2000*, 21, pp.647-654;
51. Ramsey, E.W.; Hodgson, M.E.; Sapkota, S.K.; Nelson, G.A. Forest impact estimated with NOAA AVHRR and LandsatTM data related to an empirical hurricane wind-field distribution. *Remote Sensing Environment*, **2001**, *77*, 279 – 292;
52. Jonikavicius, D.; Mozgeris, G.; Rapid assessment of wind storm-caused forest damage using satellite images and stand-wise forest inventory data. *iForest*, **2013**, 6, pp.50–155;
53. Hermosilla, T.; Wulder, M.A.; White, J.C.; Coops, N.C.; Hobart, G.W. Regional detection, characterization, and attribution of annual forest change from 1984 to 2012 using Landsat-derived time-series metrics. *Remote Sensing Environment*, **2015,** 170, pp. 121–132;
54. Jackson, R.G.; Foody, G.M.; Quine, C.P. Characterising windthrown gaps from fine spatial resolution remotely sensed data. *Forest Ecology and Management*, **2000**, 135, pp.253 - 260.
55. Malthus, T.J.; Suárez, J.C.; Woodhouse, I.H.; Shaw, D.T. Review of remote sensing in commercial forestry. Forestry Commission. Forest research internal report, 2002.
56. Suárez, J.C.; Ontiveros, C.; Smith, S.; Snape, S. Use of airborne LiDAR and aerial photography in the estimation of individual tree heights in forestry. *Computers and Geosciences*, **2005**, 31(2), pp.253-262.
57. Melesse, A.M.; Weng, Q.; Thenkabail, P.S.; Senay, G.B. Remote Sensing Sensors and Applications in Environmental Resources Mapping and Modelling. *Sensors*, **2007**, 7, pp. 3209-3241.
58. European Space Agency. Available online: https://earth.esa.int
59. Land info. Available online: http://www.landinfo.com/,
60. Gancz, V.; Apostol, B.; Petrila, M.; Lorent, A. Detectarea cu ajutorul imaginilor satelitare a doborâturilor de vânt și evaluarea efectelor acestora. *Rev. pădur.* **2010**, Nov. 01. Available online: http://www.revistapadurilor.ro/(16713) accessed on 2016-05-19.
61. Zhu, Z.; Woodcock, C.E. Object-based cloud and cloud shadow detection in Landsat imagery. *Remote Sensing of the Environment*. **2012**, 118, pp.83-94.
62. Goodwin, N.R.; Collett, L.J.; Denham, R.J.; Flood, N.; Tindall, D. Cloud and cloud shadow screening across Queensland, Australia: An automated method for Landsat TM/ETM+ time series. *Remote Sensing of Environment*, **2013**, 134, pp. 50–65. DOI:10.1016/j.rse.2013.02.019
63. Glovis. Available online: http://glovis.usgs.gov/
64. Duché,Y.; Savazzi, R.; Reymond, B., Carnus, E., Crespy, L. Cartographie de la sensibilité de la végétation aux incendies de forêts en région méditerranéenne: apports des images satellites et limites d'usage. *RDV techniques,* **2011,** nr.32 - printemps 2011 – ONF.
65. Chander, G.; Markham, B.L. Revised Landsat-5 TM Radiometric Calibration Procedures and Post calibration Dynamic Ranges. *IEEE Transactions on Geosciences and Remote Sensing*,**2003**, 41, 11, pp.2674-2677.
66. Chander, G.; Markham, B.L.; Helder, D.L. Summary of current radiometric calibration coefficients for Landsat MSS, TM, ETM+, and EO-1 ALI sensors, *Remote Sens. Environ.*, **2009, 113**, 893–903.
67. Zhu, Z.; Woodcock, C.E. Continuous change detection and classification of land cover using all available Landsat data. *Remote Sens. Environ*. **2014**,144, pp.152-171.
68. Martinuzzi, S.; Gould, W.A.; Ramos-Gonzalez, O.M. Creating Cloud-Free Landsat ETM+ Data Sets in Tropical Landscapes: Cloud and Cloud-Shadow Removal. General Technical Report, IITF-GTR-32. USDA, Forest Service, International Institute of Tropical Forestry. 2007.
69. Kennedy, R.E.; Cohen, W.B.; Moisen, G.G.; Goward, S.N.; Wulder, M.; Powell, S.L.; Masek, J.G.;Huang, C.; Healey, S P. A sample design for Landsat-based estimation of national trends in forest disturbance and

regrowth. NASA joint workshop on biodiversity, terrestrial ecology, and related applied sciences. August 21– 25, 2006, College Park, MD.

70. Kuemmerle, T.; Hostert, P.; Radeloff, V.C.; Perzanowski, K.,; Kruhlov, I. Post- socialist forest disturbance in the Carpathian border region of Poland, Slovakia, and Ukraine. *Ecol. Appl.* **2007**, 17, pp.1279–1295.
71. Masek, J.G.; Huang, C.; Wolfe, R.; Cohen, W.; Hall, F.; Kutler, J.; Nelson, P. North American forest disturbance mapped from decadal Landsat record. *Remote Sens. Environ*. **2008**,112, pp.2914–2926. DOI: 10.1016/j.rse.2008.02.010
72. Kuemmerle, T.; Chaskovskyy, O.; Knorn, J.; Radeloff, V.C.; Kruhlov, I.; Keeton, W.S.; Hostert, P. Forest cover change and illegal logging in the Ukrainian Carpathians in the transition period from 1988 to 2007. *Remote Sens. Environ*. **2009**,113, pp.1194–1207.
73. Neigh, Christopher S R, Bolton, Douglas K., Diabate, Mouhamad, Williams, Jennifer J. Carvalhais, Nuno. An automated approach to map the history of forest disturbance from insect mortality and harvest with landsat time-series data. Remote Sens. 2014, 6, 2782-2808; doi:10.3390/rs6042782
74. Frantz, D.; Röder, A.; Udelhoven, T.; Schmidt, M. Forest disturbance mapping using dense synthetic Landsat/MODIS time-series and permutation-based disturbance index detection. *Remote Sensing*, 2016, 8(4). DOI: 10.3390/rs8040277.
75. Furtuna, P. Temporal and spatial variation of forest coverage in apuseni natural park, 2000-2014 period. *Geographia Technica*, 2017, 12(1). DOI: 10.21163/GT_2017.121.05
76. Darwish, A.; Leukert, K.; Reinhardt, W. Image Segmentation for The Purpose of Object-Based Classification, Geoscience and Remote Sensing Symposium. IGARSS '03. Proceedings. *IEEE International*. **2003**, 3 pp.2039 – 2041. DOI:10.1109/IGARSS.2003.1294332.
77. Pekkarinen, A., Image segmentation in multi-source forest inventory. Finnish Forest Research Institute. Research papers 926, 2004, ISBN 952-10-2003-2.
78. Yoshino, K.; Kawaguchi, S.; Kanda, F., Tsai, F. Very High Resolution Plant Community Mapping at High Moor, Kushiro Wetland. *Photographic engineering and remote sensing*, **2014**, 80 (9), pp.895-905.
79. Geoportail. Available online: http://www.geoportail.gouv.fr/
80. Institut national de l'information géographique et forestière. Available online: http://professionnels.ign.fr
81. Inventaire forestiere. Available online: http://inventaire-forestier.ign.fr/spip/
82. Carmen - L'application cartographique au service des données environnementales. Available online http://carmen.carmencarto.fr/
83. Inventaire Forestier National - IFN (2003), Les tempêtes de décembre 1999 bilan national et Enseignements, L'IF nº 2, décembre 2003.

Supplementary Materials:

Table S1. Polygons obtained after running the detection algorithm.

	OBJCTID	Id	Shap_Lg	Area_m²	Ara_ha	X (decimal degrees)	Y (decimal degrees)	Longitude	Latitude
1	381	381	327.66	4921.4	0.4921	7.347278	49.147080	7° 20' 50.202"	49° 8' 49.486"
2	2461	2461	269.30	3290.6	0.3291	7.323385	49.070599	7° 19' 24.184"	49° 4' 14.156"
3	7037	7037	1454.88	77313.3	7.7313	7.509725	48.991177	7° 30' 35.010"	48° 59' 28.237"
4	7462	7462	169.76	1228.8	0.1229	7.515414	48.989874	7° 30' 55.490"	48° 59' 23.547"
5	7482	7482	120.00	900.0	0.0900	7.514831	48.989579	7° 30' 53.391"	48° 59' 22.484"
6	7601	7601	256.60	2963.2	0.2963	7.511610	48.988011	7° 30' 41.797"	48° 59' 16.838"
7	8227	8227	219.57	2034.1	0.2034	7.560925	48.979285	7° 33' 39.328"	48° 58' 45.428"
8	8925	8925	169.77	1229.0	0.1229	7.567033	48.970118	7° 34' 1.319"	48° 58' 12.423"
9	9353	9353	213.01	2132.2	0.2132	7.410459	48.961315	7° 24' 37.651"	48° 57' 40.735"
10	9363	9363	1748.00	78665.9	7.8666	7.407721	48.963144	7° 24' 27.794"	48° 57' 47.317"
11	10361	10361	224.28	2418.1	0.2418	7.188378	48.938636	7° 11' 18.162"	48° 56' 19.089"
12	11771	11771	489.00	10211.5	1.0211	7.404978	48.913743	7° 24' 17.922"	48° 54' 49.473"
13	11823	11823	432.87	8105.0	0.8105	7.400416	48.912271	7° 24' 1.499"	48° 54' 44.177"
14	11863	11863	224.28	2418.1	0.2418	7.396563	48.910951	7° 23' 47.627"	48° 54' 39.425"
15	11884	11884	224.28	2418.1	0.2418	7.394142	48.909838	7° 23' 38.911"	48° 54' 35.418"
16	11936	11936	213.01	2132.2	0.2132	7.388374	48.908921	7° 23' 18.148"	48° 54' 32.115"
17	11937	11937	362.36	7525.5	0.7526	7.392273	48.909277	7° 23' 32.181"	48° 54' 33.398"
18	11975	11975	120.00	900.0	0.0900	7.395239	48.908091	7° 23' 42.861"	48° 54' 29.127"
19	11992	11992	172.66	1046.0	0.1046	7.394726	48.907814	7° 23' 41.014"	48° 54' 28.130"
20	12014	12014	322.64	4991.2	0.4991	7.388727	48.907413	7° 23' 19.416"	48° 54' 26.686"
21	12063	12063	268.59	3297.5	0.3298	7.387090	48.906768	7° 23' 13.525"	48° 54' 24.364"
22	12084	12084	170.22	1214.9	0.1215	7.385695	48.906354	7° 23' 8.502"	48° 54' 22.875"
23	12205	12205	180.00	1800.0	0.1800	7.382662	48.904542	7° 22' 57.582"	48° 54' 16.350"
24	12453	12453	120.00	900.0	0.0900	7.216358	48.895476	7° 12' 58.889"	48° 53' 43.715"
25	13489	13489	169.77	1229.0	0.1229	7.284117	48.852362	7° 17' 2.823"	48° 51' 8.504"
26	13508	13508	322.66	4274.5	0.4275	7.282140	48.851920	7° 16' 55.705"	48° 51' 6.912"

doi:10.20944/preprints201709.0038.v1

27	13525	13525	376.43	5786.9	0.5787	7.285366	48.850807	7° 17' 7.317"	48° 51' 2.905"
28	13540	13540	267.12	2878.8	0.2879	7.281793	48.849646	7° 16' 54.453"	48° 50' 58.727"
29	13556	13556	120.00	900.0	0.0900	7.279782	48.848400	7° 16' 47.215"	48° 50' 54.239"
30	13559	13559	120.00	900.0	0.0900	7.280200	48.848136	7° 16' 48.719"	48° 50' 53.289"
31	13568	13568	120.00	900.0	0.0900	7.280618	48.847872	7° 16' 50.224"	48° 50' 52.340"
32	14882	14882	120.00	900.0	0.0900	7.275157	48.768712	7° 16' 30.565"	48° 46' 7.363"
33	15198	15198	265.37	3187.2	0.3187	7.349408	48.748613	7° 20' 57.868"	48° 44' 55.007"
34	15277	15277	209.69	1972.1	0.1972	7.281863	48.743617	7° 16' 54.708"	48° 44' 37.022"
35	15289	15289	360.00	7200.0	0.7200	7.282939	48.740911	7° 16' 58.580"	48° 44' 27.279"
36	15298	15298	334.52	6612.2	0.6612	7.282392	48.742647	7° 16' 56.610"	48° 44' 33.527"
37	16608	16608	833.26	32473.6	3.2474	7.140469	48.687928	7° 8' 25.688"	48° 41' 16.542"
38	16672	16672	718.37	18109.8	1.8110	7.142110	48.685686	7° 8' 31.594"	48° 41' 8.470"
39	16674	16674	299.45	4802.4	0.4802	7.143827	48.685477	7° 8' 37.779"	48° 41' 7.716"
40	16938	16938	120.00	900.0	0.0900	7.132053	48.674985	7° 7' 55.392"	48° 40' 29.944"
41	16939	16939	264.55	4093.0	0.4093	7.132919	48.675171	7° 7' 58.509"	48° 40' 30.615"
42	16963	16963	643.55	10507.4	1.0507	7.130703	48.674397	7° 7' 50.530"	48° 40' 27.830"
43	16981	16981	169.77	1228.9	0.1229	7.132906	48.673229	7° 7' 58.463"	48° 40' 23.623"
44	17028	17028	661.69	15097.1	1.5097	7.128864	48.671886	7° 7' 43.911"	48° 40' 18.788"
45	17106	17106	789.71	12482.8	1.2483	7.132993	48.670633	7° 7' 58.775"	48° 40' 14.278"
46	17144	17144	285.23	3842.1	0.3842	7.134045	48.668716	7° 8' 2.562"	48° 40' 7.377"
47	19017	19017	256.11	3961.9	0.3962	7.069609	48.621487	7° 4' 10.592"	48° 37' 17.354"
48	19411	19411	1777.12	129798.2	12.9798	7.157301	48.618670	7° 9' 26.284"	48° 37' 7.213"
49	19458	19458	212.17	2112.0	0.2112	7.183347	48.615975	7° 11' 0.048"	48° 36' 57.511"
50	19802	19802	120.00	900.0	0.0900	6.997850	48.606063	6° 59' 52.259"	48° 36' 21.825"
51	20815	20815	163.00	1255.7	0.1256	7.082725	48.589829	7° 4' 57.811"	48° 35' 23.383"
52	20860	20860	412.02	6571.0	0.6571	7.081275	48.589519	7° 4' 52.591"	48° 35' 22.268"
53	20890	20890	300.00	5400.0	0.5400	7.082554	48.588611	7° 4' 57.193"	48° 35' 19.000"

doi:10.20944/preprints201709.0038.v1

54	20948	20948	163.00	1255.7	0.1256	7.083998	48.587691	7° 5' 2.393"	48° 35' 15.686"
55	21005	21005	120.00	900.0	0.0900	7.085278	48.586497	7° 5' 7.001"	48° 35' 11.390"
56	21043	21043	120.00	900.0	0.0900	7.147099	48.586969	7° 8' 49.555"	48° 35' 13.089"
57	21076	21076	317.56	5114.4	0.5114	7.086101	48.585656	7° 5' 9.964"	48° 35' 8.363"
58	21155	21155	224.98	2781.7	0.2782	7.147809	48.585483	7° 8' 52.111"	48° 35' 7.738"
59	21213	21213	120.00	900.0	0.0900	7.146374	48.584528	7° 8' 46.947"	48° 35' 4.302"
60	21226	21226	200.25	2515.0	0.2515	7.127448	48.584163	7° 7' 38.813"	48° 35' 2.988"
61	21241	21241	256.11	3961.9	0.3962	7.149951	48.584210	7° 8' 59.823"	48° 35' 3.156"
62	21267	21267	6439.64	328767.0	9.1852	7.098719	48.587042	7° 5' 55.387"	48° 35' 13.352"
63	21274	21274	300.00	5400.0	0.5400	7.127102	48.583137	7° 7' 37.568"	48° 34' 59.292"
64	21277	21277	223.00	3055.7	0.3056	7.164146	48.583599	7° 9' 50.927"	48° 35' 0.955"
65	21452	21452	550.10	12540.6	1.2541	7.168475	48.581431	7° 10' 6.508"	48° 34' 53.153"
66	22356	22356	120.00	900.0	0.0900	7.121400	48.566849	7° 7' 17.042"	48° 34' 0.658"
67	22443	22443	577.47	15575.5	1.5575	7.119109	48.566457	7° 7' 8.794"	48° 33' 59.245"
68	22551	22551	120.00	900.0	0.0900	7.334484	48.567161	7° 20' 4.143"	48° 34' 1.779"
69	22958	22958	430.87	9278.3	0.9278	7.035810	48.556293	7° 2' 8.916"	48° 33' 22.654"
70	23024	23024	480.00	10800.0	1.0800	7.035847	48.555030	7° 2' 9.050"	48° 33' 18.107"
71	23038	23038	169.76	1228.8	0.1229	7.031971	48.554678	7° 1' 55.096"	48° 33' 16.842"
72	23094	23094	954.76	33320.0	3.3320	6.978291	48.552374	6° 58' 41.846"	48° 33' 8.547"
73	23116	23116	823.73	26656.1	2.6656	7.029786	48.553955	7° 1' 47.230"	48° 33' 14.238"
74	23143	23143	349.59	5576.1	0.5576	6.975188	48.553122	6° 58' 30.676"	48° 33' 11.238"
75	23176	23176	163.00	1255.7	0.1256	7.078820	48.553326	7° 4' 43.752"	48° 33' 11.974"
76	23187	23187	224.28	2418.2	0.2418	7.077782	48.553047	7° 4' 40.016"	48° 33' 10.970"
77	23220	23220	300.00	5400.0	0.5400	7.075992	48.552469	7° 4' 33.572"	48° 33' 8.889"
78	23288	23288	354.87	6187.5	0.6187	7.079457	48.551531	7° 4' 46.044"	48° 33' 5.512"
79	23302	23302	163.00	1255.7	0.1256	7.082152	48.551222	7° 4' 55.747"	48° 33' 4.400"
80	23380	23380	168.01	1393.6	0.1394	7.095778	48.549970	7° 5' 44.801"	48° 32' 59.891"

doi:10.20944/preprints201709.0038.v1

81	23389	23389	438.23	8861.8	0.8862	7.079972	48.549914	7° 4' 47.899"	48° 32' 59.690"
82	23458	23458	277.89	3387.5	0.3387	7.081279	48.548692	7° 4' 52.604"	48° 32' 55.291"
83	23526	23526	1684.01	53471.8	5.3472	7.095052	48.550939	7° 5' 42.189"	48° 33' 3.380"
84	23607	23607	621.52	14512.3	1.4512	7.095847	48.546374	7° 5' 45.050"	48° 32' 46.947"
85	23827	23827	2436.83	166363.4	3.8650	7.002467	48.541006	7° 0' 8.881"	48° 32' 27.620"
86	23843	23843	522.95	13622.9	1.3623	6.994330	48.540124	6° 59' 39.587"	48° 32' 24.445"
87	24072	24072	653.42	16176.8	1.6177	6.987321	48.536292	6° 59' 14.355"	48° 32' 10.652"
88	24075	24075	227.61	1857.7	0.1858	7.015204	48.536142	7° 0' 54.734"	48° 32' 10.112"
89	24091	24091	224.28	2418.2	0.2418	6.945620	48.534553	6° 56' 44.233"	48° 32' 4.389"
90	24116	24116	168.12	1349.7	0.1350	7.018118	48.535307	7° 1' 5.227"	48° 32' 7.105"
91	24196	24196	266.95	3199.2	0.3199	7.018890	48.533683	7° 1' 8.003"	48° 32' 1.259"
92	24226	24226	328.62	5129.5	0.5130	6.951903	48.531878	6° 57' 6.850"	48° 31' 54.762"
93	24286	24286	978.26	42216.8	4.2217	6.960387	48.531902	6° 57' 37.393"	48° 31' 54.848"
94	24322	24322	170.22	1214.9	0.1215	6.949084	48.529375	6° 56' 56.704"	48° 31' 45.751"
95	24740	24740	257.66	3102.6	0.3103	7.081205	48.522858	7° 4' 52.337"	48° 31' 22.288"
96	24906	24906	276.77	3300.4	0.3300	7.079757	48.520636	7° 4' 47.125"	48° 31' 14.289"
97	24963	24963	120.00	900.0	0.0900	7.078473	48.519177	7° 4' 42.502"	48° 31' 9.036"
98	27756	27756	390.60	6298.4	0.6298	6.908963	48.476141	6° 54' 32.266"	48° 28' 34.108"
99	27787	27787	411.21	9407.9	0.9408	6.906792	48.475905	6° 54' 24.452"	48° 28' 33.257"
100	28074	28074	1883.34	85002.9	4.1185	6.906583	48.473189	6° 54' 23.699"	48° 28' 23.480"
101	28208	28208	286.43	4871.0	0.4871	6.904374	48.470593	6° 54' 15.746"	48° 28' 14.134"
102	28330	28330	521.79	10777.3	1.0777	6.907999	48.469531	6° 54' 28.797"	48° 28' 10.312"
103	28533	28533	328.28	4408.7	0.4409	6.944120	48.468323	6° 56' 38.832"	48° 28' 5.964"
104	28662	28662	306.17	4614.9	0.4615	6.945653	48.467190	6° 56' 44.352"	48° 28' 1.885"
105	28837	28837	270.85	3900.6	0.3901	6.976134	48.465983	6° 58' 34.082"	48° 27' 57.538"
106	28967	28967	302.67	5076.5	0.5077	6.973708	48.464862	6° 58' 25.349"	48° 27' 53.503"
107	28969	28969	300.00	5400.0	0.5400	6.980086	48.464589	6° 58' 48.309"	48° 27' 52.520"

doi:10.20944/preprints201709.0038.v1

108	29170	29170	485.16	14181.3	1.4181	6.978799	48.462471	6° 58' 43.676"	48° 27' 44.894"
109	29222	29222	684.90	22449.5	2.2450	6.972086	48.462778	6° 58' 19.511"	48° 27' 46.001"
110	29387	29387	324.64	5958.0	0.5958	6.977524	48.460374	6° 58' 39.088"	48° 27' 37.347"
111	29522	29522	172.66	1046.0	0.1046	6.975760	48.458542	6° 58' 32.736"	48° 27' 30.751"
112	31127	31127	169.76	1228.8	0.1229	6.950751	48.441517	6° 57' 2.705"	48° 26' 29.461"
113	32858	32858	360.00	7200.0	0.7200	6.910702	48.424617	6° 54' 38.526"	48° 25' 28.621"
114	33039	33039	501.15	10310.9	1.0311	6.912671	48.423554	6° 54' 45.617"	48° 25' 24.794"
115	33117	33117	406.52	5990.2	0.5990	6.915411	48.422283	6° 54' 55.480"	48° 25' 20.219"
116	33207	33207	163.00	1255.7	0.1256	6.925611	48.421648	6° 55' 32.198"	48° 25' 17.932"
117	33408	33408	211.92	2085.1	0.2085	6.926289	48.419724	6° 55' 34.640"	48° 25' 11.005"
118	35168	35168	579.26	18669.7	1.8670	6.798052	48.404261	6° 47' 52.988"	48° 24' 15.341"
119	35893	35893	428.15	10147.4	1.0147	6.797606	48.398554	6° 47' 51.382"	48° 23' 54.795"
120	36245	36245	224.28	2418.2	0.2418	6.840897	48.395059	6° 50' 27.231"	48° 23' 42.211"
121	36312	36312	300.00	5400.0	0.5400	6.798424	48.395126	6° 47' 54.326"	48° 23' 42.452"
122	36318	36318	243.14	3019.8	0.3020	6.839625	48.394567	6° 50' 22.651"	48° 23' 40.440"
123	36505	36505	212.18	2112.1	0.2112	6.955297	48.396221	6° 57' 19.068"	48° 23' 46.395"
124	36598	36598	675.47	23152.2	2.3152	6.797437	48.393078	6° 47' 50.773"	48° 23' 35.080"
125	36630	36630	322.65	4785.1	0.4785	6.836460	48.393209	6° 50' 11.255"	48° 23' 35.554"
126	36663	36663	300.00	5400.0	0.5400	6.795116	48.391958	6° 47' 42.417"	48° 23' 31.049"
127	36893	36893	316.54	5611.9	0.5612	6.834163	48.391695	6° 50' 2.986"	48° 23' 30.103"
128	37125	37125	439.35	9668.5	0.9669	6.831618	48.390070	6° 49' 53.826"	48° 23' 24.251"
129	37457	37457	120.00	900.0	0.0900	6.807143	48.385575	6° 48' 25.716"	48° 23' 8.070"
130	37496	37496	120.00	900.0	0.0900	6.806750	48.385298	6° 48' 24.300"	48° 23' 7.072"
131	37674	37674	733.46	16331.9	1.6332	6.805255	48.385085	6° 48' 18.919"	48° 23' 6.307"
132	38162	38162	120.00	900.0	0.0900	6.738969	48.378587	6° 44' 20.287"	48° 22' 42.911"
133	38311	38311	120.00	900.0	0.0900	6.737814	48.377214	6° 44' 16.130"	48° 22' 37.971"
134	38421	38421	120.00	900.0	0.0900	6.720050	48.375784	6° 43' 12.182"	48° 22' 32.821"

doi:10.20944/preprints201709.0038.v1

135	38734	38734	120.00	900.0	0.0900	6.738386	48.373447	6° 44' 18.190"	48° 22' 24.408"
136	38946	38946	169.77	1229.0	0.1229	6.739053	48.371588	6° 44' 20.591"	48° 22' 17.718"
137	39216	39216	603.36	13616.3	1.3616	6.737833	48.369714	6° 44' 16.198"	48° 22' 10.969"
138	39657	39657	170.22	1214.9	0.1215	6.734896	48.365836	6° 44' 5.626"	48° 21' 57.009"
139	39784	39784	410.27	7473.3	0.7473	6.737050	48.365014	6° 44' 13.381"	48° 21' 54.050"
140	41319	41319	120.00	900.0	0.0900	7.199109	48.359451	7° 11' 56.791"	48° 21' 34.025"
141	41613	41613	168.12	1349.7	0.1350	7.146976	48.356314	7° 8' 49.112"	48° 21' 22.732"
142	43190	43190	120.00	900.0	0.0900	7.317063	48.344233	7° 19' 1.429"	48° 20' 39.240"
143	46284	46284	212.18	2112.1	0.2112	7.033681	48.311023	7° 2' 1.250"	48° 18' 39.684"
144	46527	46527	598.96	14064.8	1.4065	7.032518	48.309014	7° 1' 57.066"	48° 18' 32.450"
145	46762	46762	1328.11	54443.6	3.0803	7.029074	48.306753	7° 1' 44.667"	48° 18' 24.310"
146	46825	46825	907.12	24968.1	0.9474	7.026662	48.305276	7° 1' 35.982"	48° 18' 18.994"
147	46919	46919	168.01	1393.6	0.1394	7.173274	48.305336	7° 10' 23.786"	48° 18' 19.211"
148	47124	47124	528.63	15167.4	1.5167	7.166364	48.303774	7° 9' 58.910"	48° 18' 13.588"
149	47204	47204	360.00	7200.0	0.7200	6.700044	48.293733	6° 42' 0.158"	48° 17' 37.439"
150	48931	48931	990.36	27239.2	1.7510	6.758676	48.276533	6° 45' 31.232"	48° 16' 35.518"
151	49079	49079	662.65	16955.6	1.6956	6.786183	48.275179	6° 47' 10.259"	48° 16' 30.643"
152	49080	49080	265.37	3187.2	0.3187	6.789455	48.274633	6° 47' 22.038"	48° 16' 28.680"
153	50527	50527	120.00	900.0	0.0900	7.190664	48.266198	7° 11' 26.391"	48° 15' 58.311"
154	50528	50528	233.55	3314.8	0.3315	7.192318	48.266298	7° 11' 32.343"	48° 15' 58.673"
155	50560	50560	505.34	12019.4	1.2019	7.194604	48.266396	7° 11' 40.575"	48° 15' 59.027"
156	50730	50730	265.37	3187.2	0.3187	7.189708	48.264628	7° 11' 22.950"	48° 15' 52.662"
157	50871	50871	348.02	6707.5	0.6708	7.061401	48.261315	7° 3' 41.043"	48° 15' 40.735"
158	50873	50873	355.93	6448.4	0.6448	7.188392	48.263273	7° 11' 18.211"	48° 15' 47.784"
159	53148	53148	227.83	1949.7	0.1950	7.033794	48.241288	7° 2' 1.657"	48° 14' 28.638"
160	53287	53287	698.67	14754.4	1.4754	7.034697	48.239654	7° 2' 4.909"	48° 14' 22.753"
161	53390	53390	251.91	3318.7	0.3319	7.036319	48.238000	7° 2' 10.750"	48° 14' 16.799"

doi:10.20944/preprints201709.0038.v1

162	53446	53446	168.13	1349.9	0.1350	7.039235	48.235648	7° 2' 21.244"	48° 14' 8.334"
163	53472	53472	371.44	5772.5	0.5772	7.037205	48.237221	7° 2' 13.939"	48° 14' 13.997"
164	53591	53591	168.02	1393.7	0.1394	7.038172	48.236322	7° 2' 17.419"	48° 14' 10.758"
165	56532	56532	1858.75	73516.3	0.5567	6.669043	48.202887	6° 40' 8.556"	48° 12' 10.392"
166	59374	59374	170.22	1215.0	0.1215	7.239241	48.188421	7° 14' 21.269"	48° 11' 18.316"
167	59661	59661	637.30	24506.0	2.4506	7.236356	48.186760	7° 14' 10.881"	48° 11' 12.334"
168	59763	59763	352.86	5938.6	0.5939	7.233649	48.185838	7° 14' 1.138"	48° 11' 9.017"
169	59832	59832	224.27	2418.1	0.2418	7.238307	48.187866	7° 14' 17.904"	48° 11' 16.319"
170	59855	59855	212.17	2112.0	0.2112	7.232139	48.184876	7° 13' 55.701"	48° 11' 5.554"
171	59999	59999	212.17	2112.0	0.2112	7.232580	48.183803	7° 13' 57.286"	48° 11' 1.691"
172	65019	65019	1299.96	60812.4	6.0812	6.892683	48.126341	6° 53' 33.660"	48° 7' 34.827"
173	66819	66819	120.00	900.0	0.0900	7.046643	48.130768	7° 2' 47.914"	48° 7' 50.766"
174	66870	66870	180.00	1800.0	0.1800	7.046255	48.130357	7° 2' 46.519"	48° 7' 49.284"
175	66952	66952	120.00	900.0	0.0900	7.045475	48.129669	7° 2' 43.710"	48° 7' 46.807"
176	67152	67152	240.00	3600.0	0.3600	7.044302	48.127831	7° 2' 39.488"	48° 7' 40.191"
177	67234	67234	390.24	5818.0	0.5818	7.044891	48.128745	7° 2' 41.609"	48° 7' 43.481"
178	67430	67430	335.42	4966.8	0.4967	7.043572	48.126814	7° 2' 36.861"	48° 7' 36.529"
179	67497	67497	240.00	2700.0	0.2700	7.043221	48.125311	7° 2' 35.597"	48° 7' 31.121"
180	67551	67551	180.00	1800.0	0.1800	7.042431	48.124893	7° 2' 32.751"	48° 7' 29.615"
181	67582	67582	224.28	2418.2	0.2418	7.047014	48.131375	7° 2' 49.251"	48° 7' 52.951"
182	67585	67585	224.28	2418.2	0.2418	7.043302	48.125599	7° 2' 35.886"	48° 7' 32.155"
183	67652	67652	267.93	3090.3	0.3090	7.042302	48.123969	7° 2' 32.288"	48° 7' 26.287"
184	67685	67685	163.00	1255.7	0.1256	6.895007	48.121207	6° 53' 42.026"	48° 7' 16.344"
185	67772	67772	120.00	900.0	0.0900	6.893437	48.120503	6° 53' 36.375"	48° 7' 13.811"
186	67898	67898	219.57	2034.2	0.2034	6.887958	48.119675	6° 53' 16.650"	48° 7' 10.830"
187	67931	67931	169.76	1228.8	0.1229	6.884588	48.119380	6° 53' 4.515"	48° 7' 9.769"
188	70038	70038	1846.30	84529.5	2.1201	6.646952	48.099448	6° 38' 49.029"	48° 5' 58.011"

doi:10.20944/preprints201709.0038.v1

189	70760	70760	644.05	14818.3	1.4818	6.821553	48.094559	6° 49' 17.591"	48° 5' 40.413"
190	70899	70899	347.76	5710.5	0.5710	6.828641	48.093164	6° 49' 43.106"	48° 5' 35.390"
191	70981	70981	217.54	2316.4	0.2316	6.832718	48.092224	6° 49' 57.786"	48° 5' 32.005"
192	71079	71079	312.89	3487.2	0.3487	6.701415	48.087717	6° 42' 5.093"	48° 5' 15.780"
193	71084	71084	168.13	1349.9	0.1350	6.846103	48.091283	6° 50' 45.969"	48° 5' 28.617"
194	71133	71133	318.43	5590.2	0.5590	6.851443	48.091051	6° 51' 5.195"	48° 5' 27.782"
195	71558	71558	162.99	1255.7	0.1256	6.694672	48.087413	6° 41' 40.819"	48° 5' 14.687"
196	71593	71593	213.01	2132.1	0.2132	6.695531	48.086563	6° 41' 43.911"	48° 5' 11.626"
197	72632	72632	375.80	7542.6	0.7543	7.253864	48.083853	7° 15' 13.910"	48° 5' 1.872"
198	72954	72954	120.00	900.0	0.0900	7.254784	48.080673	7° 15' 17.224"	48° 4' 50.424"
199	74046	74046	560.86	15661.7	1.5662	6.480911	48.058205	6° 28' 51.281"	48° 3' 29.539"
200	74214	74214	336.55	5010.0	0.5010	6.474940	48.055932	6° 28' 29.783"	48° 3' 21.357"
201	76429	76429	314.99	4549.8	0.4550	7.092264	48.050665	7° 5' 32.152"	48° 3' 2.395"
202	76445	76445	359.81	4711.8	0.4712	6.724043	48.043516	6° 43' 26.556"	48° 2' 36.658"
203	76839	76839	162.99	1255.7	0.1256	6.626447	48.037087	6° 37' 35.209"	48° 2' 13.513"
204	77043	77043	366.82	5796.1	0.5796	6.713402	48.037348	6° 42' 48.249"	48° 2' 14.453"
205	77091	77091	168.14	1350.0	0.1350	6.715717	48.037613	6° 42' 56.582"	48° 2' 15.406"
206	77113	77113	1375.30	39462.9	3.9463	7.090971	48.046868	7° 5' 27.494"	48° 2' 48.723"
207	77429	77429	224.29	2418.5	0.2419	6.712583	48.036340	6° 42' 45.300"	48° 2' 10.823"
208	77505	77505	211.92	2085.1	0.2085	6.629977	48.033491	6° 37' 47.917"	48° 2' 0.566"
209	77571	77571	632.38	13184.9	1.3185	7.088228	48.042689	7° 5' 17.621"	48° 2' 33.679"
210	77587	77587	172.80	1295.6	0.1296	6.716405	48.037092	6° 42' 59.056"	48° 2' 13.532"
211	77836	77836	360.00	7200.0	0.7200	6.703131	48.030983	6° 42' 11.271"	48° 1' 51.539"
212	77911	77911	311.90	4424.3	0.4424	6.705636	48.030626	6° 42' 20.290"	48° 1' 50.255"
213	77965	77965	858.34	19206.7	1.9207	7.085436	48.040173	7° 5' 7.569"	48° 2' 24.624"
214	77974	77974	224.29	2418.5	0.2419	6.708790	48.030025	6° 42' 31.645"	48° 1' 48.089"
215	78022	78022	180.00	1800.0	0.1800	7.085566	48.038163	7° 5' 8.039"	48° 2' 17.388"

doi:10.20944/preprints201709.0038.v1

216	78098	78098	219.55	2033.8	0.2034	7.084501	48.037653	7° 5' 4.202"	48° 2' 15.551"
217	78195	78195	376.47	6022.5	0.6023	6.874183	48.028792	6° 52' 27.061"	48° 1' 43.652"
218	78471	78471	361.30	4965.9	0.4966	6.871796	48.029329	6° 52' 18.466"	48° 1' 45.585"
219	78553	78553	1145.74	48137.7	4.8138	6.867195	48.030042	6° 52' 1.902"	48° 1' 48.152"
220	78944	78944	335.31	5994.1	0.5994	6.876629	48.027674	6° 52' 35.865"	48° 1' 39.627"
221	79182	79182	1125.30	59875.2	3.3453	6.409031	48.017559	6° 24' 32.511"	48° 1' 3.212"
222	79200	79200	538.76	9668.9	0.9669	6.879022	48.026555	6° 52' 44.478"	48° 1' 35.599"
223	79729	79729	218.93	2467.5	0.2468	6.830954	48.020969	6° 49' 51.434"	48° 1' 15.487"
224	80060	80060	232.80	2195.7	0.2196	6.832337	48.018405	6° 49' 56.413"	48° 1' 6.259"
225	80135	80135	300.00	4500.0	0.4500	6.831154	48.017957	6° 49' 52.154"	48° 1' 4.646"
226	80269	80269	367.54	5611.9	0.5612	6.832784	48.017249	6° 49' 58.024"	48° 1' 2.098"
227	80462	80462	493.93	10697.1	1.0697	6.832227	48.016283	6° 49' 56.017"	48° 0' 58.620"
228	80504	80504	170.21	1214.7	0.1215	6.831521	48.015411	6° 49' 53.476"	48° 0' 55.480"
229	81342	81342	466.54	13245.5	1.3245	6.598190	48.005240	6° 35' 53.485"	48° 0' 18.865"
230	81629	81629	384.24	7545.9	0.7546	6.513222	48.001015	6° 30' 47.599"	48° 0' 3.655"
231	81715	81715	2942.12	172326.8	3.6673	6.679848	48.004844	6° 40' 47.452"	48° 0' 17.439"
232	81762	81762	245.30	3308.5	0.3308	6.601119	48.001926	6° 36' 4.029"	48° 0' 6.932"
233	81871	81871	169.76	1228.8	0.1229	6.456407	47.997861	6° 27' 23.065"	47° 59' 52.300"
234	82586	82586	405.02	6833.5	0.6833	6.596993	47.996275	6° 35' 49.176"	47° 59' 46.590"
235	82935	82935	483.71	10542.9	1.0543	6.597978	47.994046	6° 35' 52.721"	47° 59' 38.566"
236	83349	83349	211.92	2085.1	0.2085	6.685108	47.991903	6° 41' 6.388"	47° 59' 30.850"
237	83422	83422	608.80	17008.7	1.7009	6.657683	47.991357	6° 39' 27.658"	47° 59' 28.885"
238	83523	83523	120.00	900.0	0.0900	6.380711	47.984162	6° 22' 50.558"	47° 59' 2.983"
239	83692	83692	472.93	10273.4	1.0273	6.677225	47.989840	6° 40' 38.010"	47° 59' 23.424"
240	85133	85133	931.19	22064.8	1.5282	6.712040	47.932766	6° 42' 43.346"	47° 55' 57.959"
241	86054	86054	120.00	900.0	0.0900	6.391648	47.966594	6° 23' 29.934"	47° 57' 59.740"
242	86056	86056	321.00	4807.4	0.4807	6.398728	47.966991	6° 23' 55.420"	47° 58' 1.168"

doi:10.20944/preprints201709.0038.v1

243	86119	86119	263.03	3038.1	0.3038	6.403234	47.966478	6° 24' 11.644"	47° 57' 59.319"
244	86199	86199	209.30	2390.6	0.2391	6.392786	47.965736	6° 23' 34.031"	47° 57' 56.650"
245	86233	86233	120.00	900.0	0.0900	6.393322	47.965283	6° 23' 35.960"	47° 57' 55.018"
246	92585	92585	616.48	17300.4	1.7300	7.093626	47.934453	7° 5' 37.055"	47° 56' 4.030"
247	92626	92626	372.61	7408.7	0.7409	6.639460	47.928902	6° 38' 22.058"	47° 55' 44.047"
248	92813	92813	275.19	3381.6	0.3382	7.091395	47.931651	7° 5' 29.022"	47° 55' 53.944"
249	92847	92847	120.00	900.0	0.0900	7.090750	47.931127	7° 5' 26.699"	47° 55' 52.056"
250	93012	93012	300.00	4500.0	0.4500	7.086603	47.930302	7° 5' 11.770"	47° 55' 49.086"
251	93088	93088	221.91	2712.9	0.2713	7.089391	47.929626	7° 5' 21.806"	47° 55' 46.653"
252	93223	93223	1311.92	35292.2	3.5292	7.088526	47.929953	7° 5' 18.692"	47° 55' 47.830"
253	93291	93291	337.10	5167.5	0.5168	7.087112	47.928197	7° 5' 13.603"	47° 55' 41.511"
254	93874	93874	800.60	19383.3	1.9383	7.086103	47.925085	7° 5' 9.970"	47° 55' 30.304"
255	95141	95141	526.29	11000.6	7.5014	7.088169	47.918369	7° 5' 17.408"	47° 55' 6.127"
256	100805	100805	651.41	18439.0	1.8439	6.579443	47.864091	6° 34' 45.994"	47° 51' 50.728"
257	103531	103531	717.76	22496.0	2.2496	6.582815	47.870216	6° 34' 58.134"	47° 52' 12.777"

802

doi:10.20944/preprints201709.0038.v1

 doi:10.20944/preprints201709.0038.v1

803